DETECTION OF RADIALLY ASYMMETRIC POINT LIGHT SOURCES

by

LIANG ZHENGXIN

A THESIS SUBMITTED FOR THE DEGREE OF

B.SC. (HONS), PHYSICS

NATIONAL UNIVERSITY OF SINGAPORE

2024

Supervisor:
Professor Christian Kurtsiefer

Acknowledgments

I would like to thank everyone who has been with me throughout this difficult but rewarding journey.

Contents

Chapter 1

Diffraction-Limited Imaging

1.1 Attempts to resolve beyond the diffraction limit

In optical imaging, the diffraction limit of an optical system is commonly known as the Rayleigh criterion [1]. For an optical system with a circular aperture, the Rayleigh criterion is defined as follows

$$\sin\theta = 1.22\frac{\lambda}{D} \tag{1.1}$$

where θ is the minimum angular separation between two points, λ is the wavelength of light, and D is the diameter of the circular aperture.

When the angular separation between two points of an object being imaged is smaller than the Rayleigh criterion, the two points are said to be diffraction-limited and thus indistinguishable in the image.

One could reduce the diffraction limit by reducing the wavelength used to image the objects. For example, in microscopy, using X-rays [2] or electrons [3]. Alternatively, one could increase the diameter of the aperture. For example, in astronomy, the construction of telescopes with large diameters [4].

Over the decade, there have been advances in techniques that could resolve beyond the diffraction limit. One such example is the use of fluorescence microscopy [5, 6]. However, these techniques require access or modification to the object under investigation, such as dyeing with a photosensitive protein. However, these techniques may not be feasible for objects such as stars or sensitive biological samples.

Around 2016 Mankei T. et al. showed that two point sources could be separated beyond the diffraction limit based on information from the image plane of an optical system and proposed Super Localization by Image inVERsion interferometry (SLIVER) [7, 8]. SLIVER is also referred to as image inversion interferometry. Using image inversion interferometry, the separation between two point sources within the diffraction limit can be determined and has been demonstrated experimentally [9].

Assuming the constraint that the object plane cannot be accessed, we propose using image inversion interferometry at the image plane to extract spatial information from a diffraction-limited point light source.

1.2 Detecting Radial Asymmetric Point Light Sources

In this thesis, we focus our investigation on radial asymmetric spatial information of a diffraction-limited point light source. Using image inversion interferometry, we present a laboratory-based proof-of-concept to demonstrate the extraction of radial asymmetric spatial information from a point light source. We then compare image inversion interferometry against a direct measurement method and present our findings.

1.3 Structure of thesis

The thesis is structured in the following:

- Chapter 2 An attempt to access information beyond diffraction-limit using image inversion interferometry.
- Chapter 3 An analysis of light sources for interference
- Chapter 4 An analysis of the generation of radial asymmetric light sources
- Chapter 5 Investigation of radial asymmetries at pupil plane.
- Chapter 6 Investigation of radial asymmetries at object plane.
- Chapter 7 Investigation into direct measurement of radial asymmetries.

Chapter 2

Image Inversion Interferometry

Interferometry is a technique used to extract information from the interference of waves such as electromagnetic waves. Examples of such information are the phase differences between the two interfering waves. Using interferometry, interferometers are devices that provide a way to measure the phase differences between two interference waves. Examples of such interferometers for electromagnetic waves are the Michelson interferometer [10] and the Mach-Zehnder interferometer [11].

2.1 Mach-Zehnder Interferometer

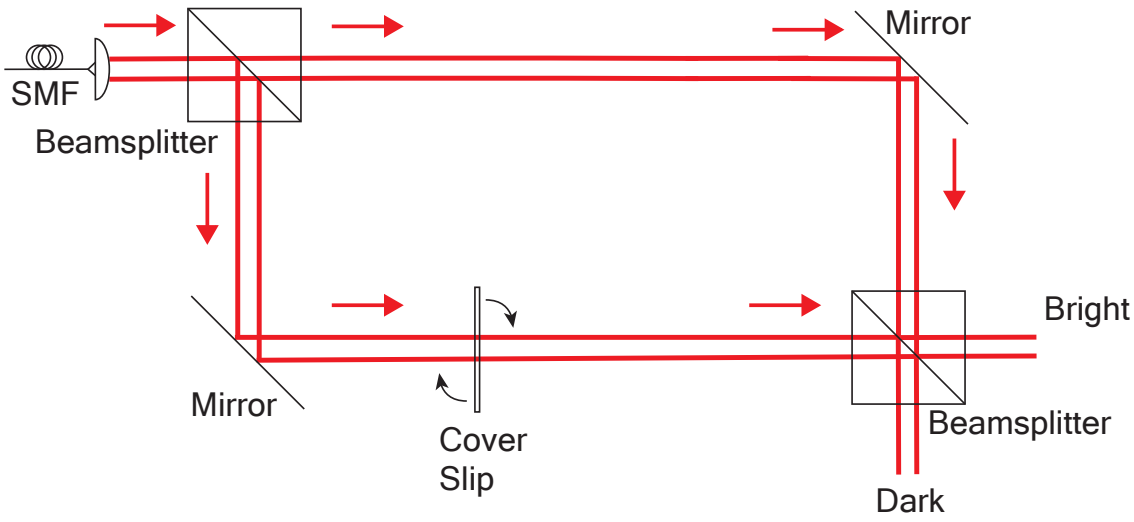

Figure 2.1: Schematic of a Mach-Zehnder interferometer

A Mach-Zehnder interferometer is a type of amplitude-splitting interferometer. A collimated light beam is split into two beams of equal intensity at a 50:50 non-

polarising beamsplitter (top left). The two beams then meet at another 50:50 non-polarising beamsplitter (bottom right) where the two beams interfere. Due to a π phase difference between the two beams at the dark output, the two beams destructively interfere. At the bright output, the two beams constructively interfere. The symmetric design of a Mach-Zehnder interferometer reduces the path difference between the two beams, allowing broadband light sources with shorter coherence lengths to interfere. In practice, a thin piece of glass (cover slip) is placed in one of the beams to increase the path length to reduce the path difference between the two beams. As the cover slip is rotated, the increase in path length can be computed using $\frac{d}{\sin\theta}$ where θ is the beam's angle of incidence on the glass. Compared to the Michelson interferometer, the two outputs of the Mach-Zehnder interferometer give additional information that would otherwise not be accessible.

By measuring the intensity of the dark and bright outputs simultaneously, the interferometric visibility can be computed in real time. Interferometric visibility gives a metric on the degree of contrast between two outputs due to interference [12].

$$V = \frac{I_{\max} - I_{\min}}{I_{\max} + I_{\min}} \tag{2.1}$$

where, V is the interferometric visibility, $I_{\max}$ intensity of the bright output, and $I_{\min}$ is the intensity of the dark output. The interferometric visibility V ranges from 0 where there is no interference between the two beams to 1 where there is perfect interference.

To maximise the interferometric visibility of a Mach-Zehnder interferometer, the phase difference between the two beams at the two outputs needs to be close to π for dark and 0 for bright. For interference to occur, the path difference between the two beams needs to be less than the temporal coherence length of the light source. The two beams must also be spatially coherent.

2.2 Image Inversion

A Mach-Zehnder interferometer allows us to compare the phase difference between the two beams. This allows one beam to act as a phase reference for the other beam, which can be modified for investigation.

In image inversion interferometry, an image inverter is added in one of the beams [8]. The image inverter inverts a property of an image along an axis. In our interest in radial asymmetries, our image inverter needs to perform a radial inversion. This can be performed using a pair of lenses positioned in a telescope configured as proposed in [13] and demonstrated in [9]. We will refer to this pair of lenses as image inversion lenses.

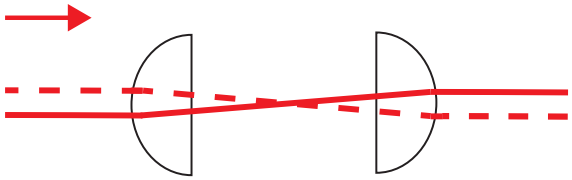

Figure 2.2: A pair lens positioned into a telescope configuration inverting the input beam along its optical axis.

If $f(\bar{r})$ describes a property of the input beam at position $\bar{r}$ from the optical axis, image inversion would result in

$$f(\bar{r}) \rightarrow f(-\bar{r}) \tag{2.2}$$

where the property $f(\bar{r})$ will be shifted to the $-\bar{r}$ position.

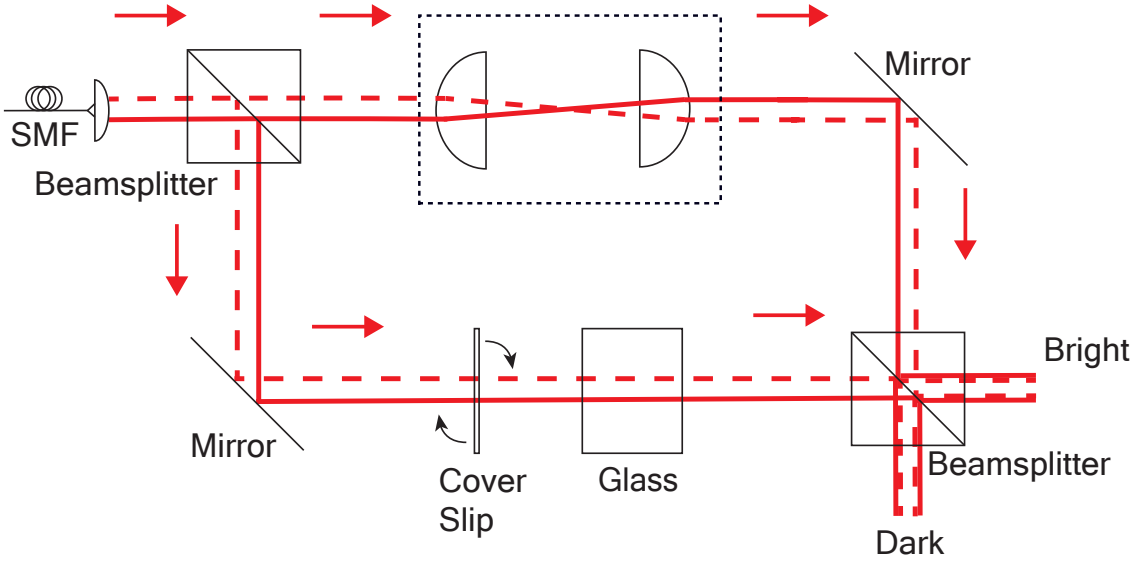

Figure 2.3: Experimental setup of image inversion interferometry which utilises a Mach-Zehnder interferometer. A pair of lenses which perform an image inversion is shown in a dotted box. This setup is similar to the experiment setup in [9]

Collimated light containing radial symmetric and asymmetric regions enters the Mach-Zehnder interferometer at the first non-polarising 50:50 beamsplitter (top left), separating the light into two beams. The transmitted beam passes through a pair of plano-convex achromatic lenses positioned in a telescope configuration with unity magnification where the beam is radially inverted. Any region with radial asymmetric properties would be radially inverted (Equation 2.2). In the reflected beam, in addition to the cover slip, light passes through another piece of glass to compensate for the increase in path difference due to the addition of the image inversion lens. The reflected and the transmitted beam then interfere at another non-polarising 50:50 beamsplitter (bottom right). The dark and bright outputs denote the two outputs of the interferometer.

Any regions containing radial asymmetric properties would not overlap and interfere at the second non-polarising beamsplitter (bottom right). Hence, these radial asymmetric regions would be separated equally at the second beamsplitter into the two outputs of the interferometer.

2.3 Radial Asymmetry

We first consider a blob with a well-defined shape to define radial symmetric and asymmetric regions.

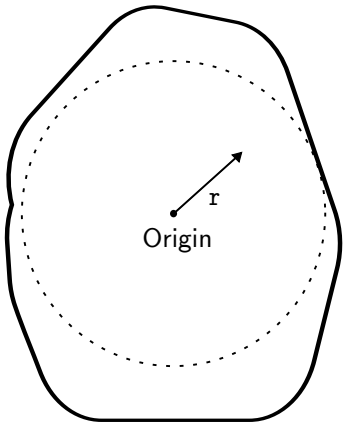

Figure 2.4: A blob with a well-defined shape is enclosed by solid black lines. If we define a point as the origin, radially symmetric regions are enclosed by dotted lines.

For any given point as the origin and a function $f(\bar{r})$ that describes a property at position vector $\bar{r}$ from the origin, radially symmetric points can be defined as

follows.

$$f(\bar{r}) = f(-\bar{r}) \tag{2.3}$$

Conversely, asymmetrical points can be defined as

$$f(\bar{r}) \neq f(-\bar{r}) \tag{2.4}$$

Therefore, when an input beam is radially inverted, radial symmetrical regions

$$f(\bar{r}) \rightarrow f(-\bar{r}) = f(\bar{r}) \tag{2.5}$$

whereas when radial asymmetrical regions are inverted,

$$f(\bar{r}) \rightarrow f(-\bar{r}) \neq f(\bar{r}) \tag{2.6}$$

These radial asymmetric regions thus do not overlap and interfere.

2.4 Noise Separation

A Mach-Zehnder interferometer could separate the majority of the noise into the bright output. By maximising the interferometric visibility of the interferometer, noise could be separated into the bright and dark outputs of the interferometer asymmetrically due to the significantly lower intensity of the dark output compared to the bright output. Thus, the dark output has a lower noise compared to the noise of the input beam into the interferometer, which is denoted by total. In our measurement, the total is the contribution from both the dark and bright outputs.

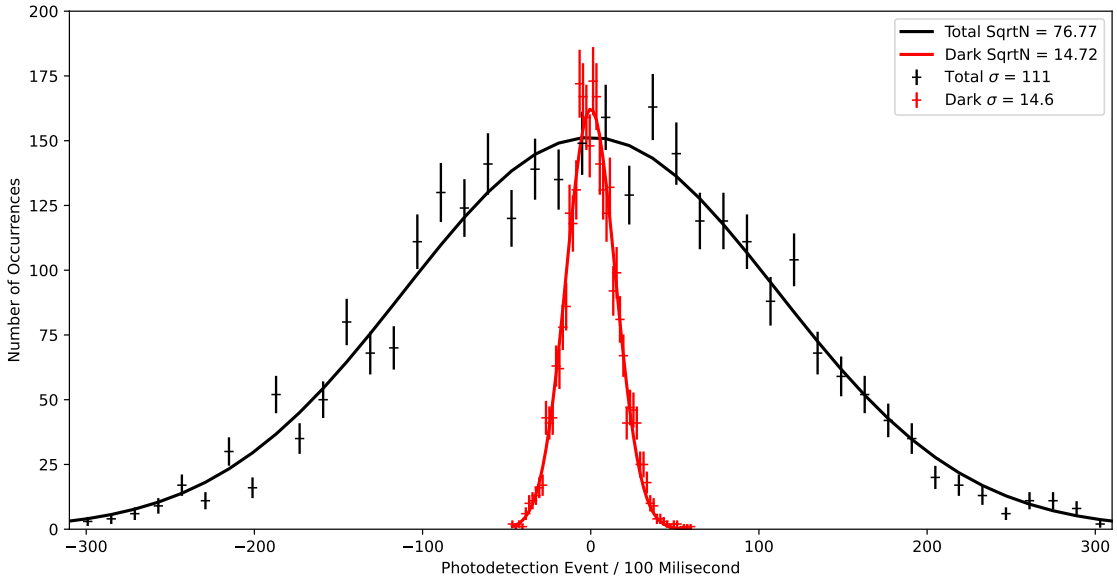

Figure 2.5: The intensity measurement denoted by total has a $\sigma = 111 \pm 2$ counts per 100 ms. The dark output of the interferometer has a $\sigma = 14.6 \pm 0.3$ counts per 100 ms

The standard deviations, σ were used to quantify the amount of noise present in both the dark output and total. The amount of noise can affect the signal-to-noise ratio of our measurements, which will be discussed in Chapter 5.

Chapter 3

Light Sources

In this chapter, we discussed the various properties of light sources for image inversion interferometry. Three light sources, a HeNe 543.5 nm laser, a Hg vapour discharge lamp, and a diode-pumped solid-state 532 nm laser, were investigated.

3.1 Properties

3.1.1 Centre Wavelength of Light Source

We chose to focus on light sources in the optical wavelengths centred around 550 nm as it is near the peak spectral efficiency of the Si detectors such as single-photon detectors and cameras. It is also in the optical region, which makes it ideal for visual alignment of the Mach-Zehnder interferometer.

3.1.2 Spectral Linewidth

For interference to occur, the optical path difference between two beams in the Mach-Zehnder interferometer Δx needs to be less than the temporal coherence length L_c of the light source [14]. The temporal coherence length L_c can be computed using

$$L_c = c\tau_c \tag{3.1}$$

where c is the speed of light and τ_c is the temporal coherence time. The temporal coherence time can be approximated for a light source with Gassuain lineshape using

$$\tau_c \approx \frac{1}{\Delta f} \tag{3.2}$$

where Δf is the frequency linewidth of a spectral line. Thus, the temporal coherence length can be approximated as

$$L_c \approx \frac{c}{\Delta f} \tag{3.3}$$

If we are able to measure the wavelength linewidth $\Delta\lambda$ of a light source, and using $c = f\lambda$ and the mean wavelength λ_c, the frequency linewidth Δf can be determined from

$$\Delta f = f_2 - f_1 \tag{3.4}$$

$$f_1 = \frac{c}{\lambda_c + \frac{\Delta\lambda}{2}} \tag{3.5}$$

$$f_2 = \frac{c}{\lambda_c - \frac{\Delta\lambda}{2}} \tag{3.6}$$

This will allow us to determine if the light source's temporal coherence length is longer than the interferometer's optical path difference allowing for interference to occur.

3.1.3 Power and Noise Output

A light source's power output P would determine the smallest percentage change in power resolvable. If we assume that the noise contribution of the light source is modelled using a Poissonian distribution [14] where N is the mean photodetection events, the amount of noise is defined as

$$\text{Noise} = \sqrt{N} \tag{3.7}$$

Each photon carries a quantum of energy and can be measured in the number of photodetection events per unit of time. Thus, it can be used as a representation of power with a scaling factor.

In image inversion interferometry, we are interested in the changes in power ΔP that occur when radial asymmetric regions do not overlap and interfere. Thus, to resolve the changes in power,

$$\frac{\Delta P}{\text{Noise}} > 1 \tag{3.8}$$

If we assume that the noise is modelled after a Poissonian distribution, the percentage of noise decreases as the number of photodetection events increases. Thus allowing smaller percentages of changes in power to be resolved.

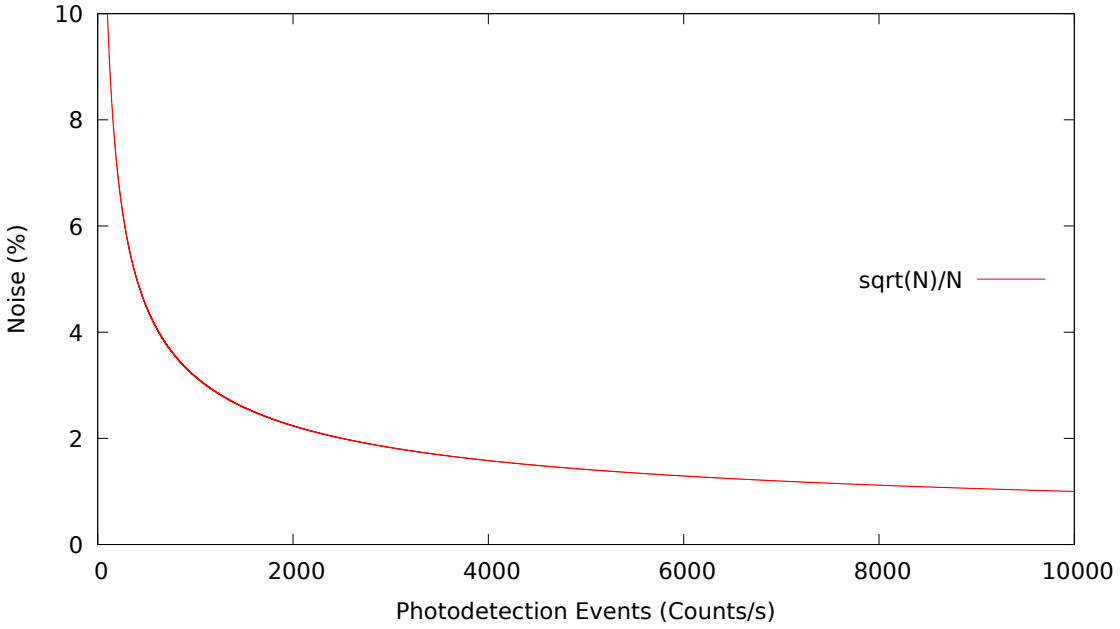

Figure 3.1: Assuming the change in power ΔP is equal to noise contribution such that the change in power is just resolved. $\frac{\Delta P}{\text{Noise}} = 1$ and noise contributions are modelled using Poissonian distribution.

However, light sources in the lab may not be modelled after a Poissonian distribution and may have other contributions of noise. Thus, to determine a light source's noise, the output power could be fitted to a Gaussian function.

$$\text{Gaussian}(P) = \frac{A}{\sigma\sqrt{2\pi}} e^{-\frac{(P-P_0)^2}{2\sigma^2}} \tag{3.9}$$

where, A is Amplitude, σ is the standard deviation, and P_0 is the mean power. Using the fitted standard deviation σ values, we will then be able to compute the percentage noise,

$$\%\text{Noise} = \frac{\sigma}{x_0} \cdot 100 \tag{3.10}$$

3.2 Light Sources

3.2.1 543.5nm HeNe Laser

A HeNe laser with a centre wavelength of 543.5 nm indicated in the specifications [15] was used as a light source. A spectrum of the HeNe laser was measured using a spectrometer to verify the laser's centre wavelength and whether it is single-emission.

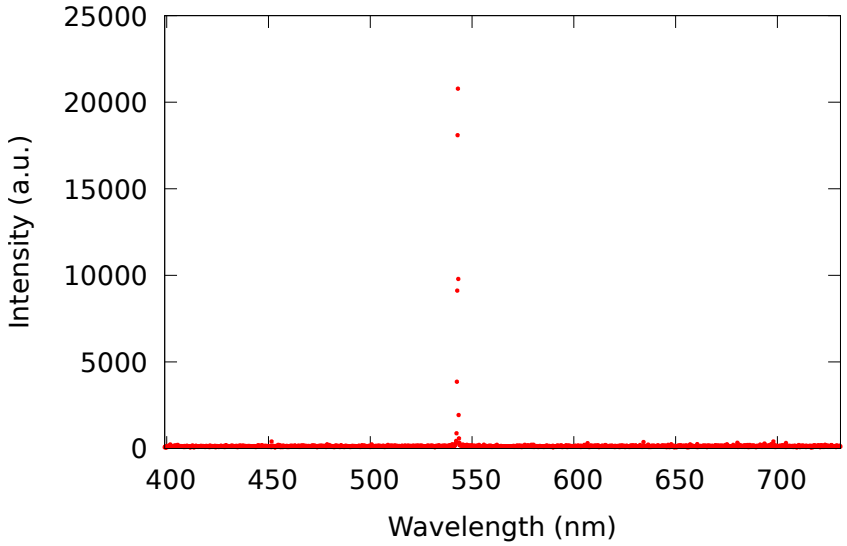

Figure 3.2: The HeNe laser has a dominant peak at around 540 nm suggesting that the laser has a single-emission line in the optical wavelengths. The spectral range of the spectrometer is $399 - 731$ nm as indicated in the wavelength calibration data sheet [16]

The dominant peak was fitted to a Gaussian function (Equation 3.9).

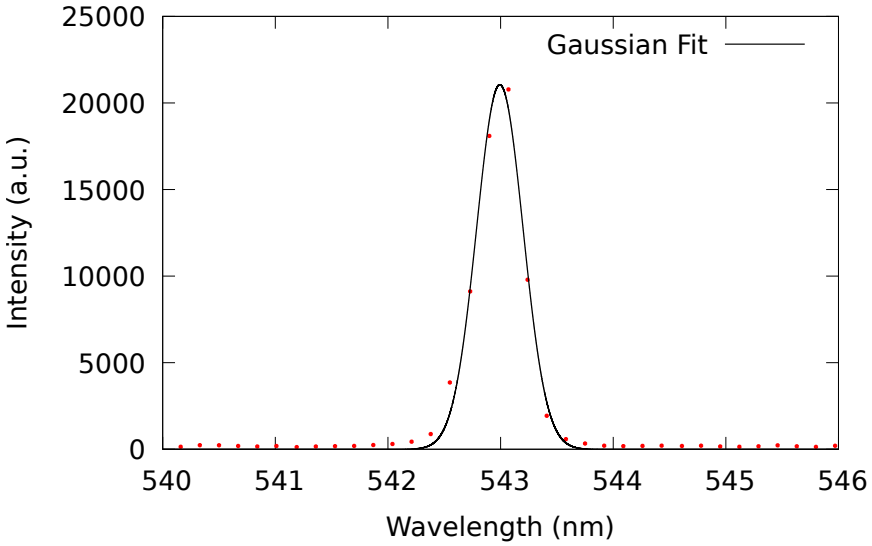

Figure 3.3: The spectrum was fitted to a Gaussian Function. Mean: $542.993 \pm 0.002\,\text{nm}$, Standard Deviation σ: $0.206 \pm 0.002\,\text{nm}$, Full-Width Half Maximum (FWHM): $0.485 \pm 0.005\,\text{nm}$, and reduced Chi-Square: 49988

The wavelength full width at half maximum is around 0.485 nm. This suggests that the resolution of the spectrometer may have limited the measurement as the HeNe laser should have a frequency linewidth on the order of GHz.

The resolution of a grating spectrometer [12] is defined as

$$R = \frac{\lambda}{\Delta\lambda} = mN \tag{3.11}$$

where R is the resolvance, λ is the center wavelength, $\Delta\lambda$ is the smallest resolvable wavelength bandwidth difference, m is the order of diffraction, and N is the number of slits illuminated by the light source.

Thus, assuming 1 mm of the diffraction grating (1200 lines/mm [16], $N = 1200$) in the spectrometer is illuminated and taking the first order diffraction ($m = 1$), the smallest wavelength resolvable $\Delta\lambda \approx 0.5\,\text{nm}$ which further suggests that the spectrum measurement is spectrometer limited.

Next, we investigated the laser's noise. The photodetection events of the HeNe laser were measured using single-photon detectors. The results were then binned into bins with a width of 169 counts/s.

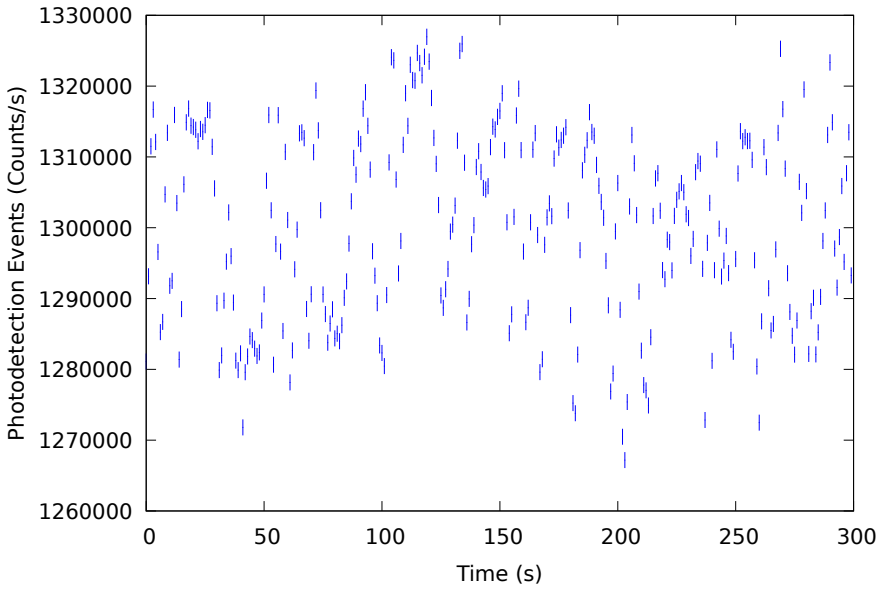

Figure 3.4: A 5 minutes measurement of HeNe laser output using single-photon detectors.

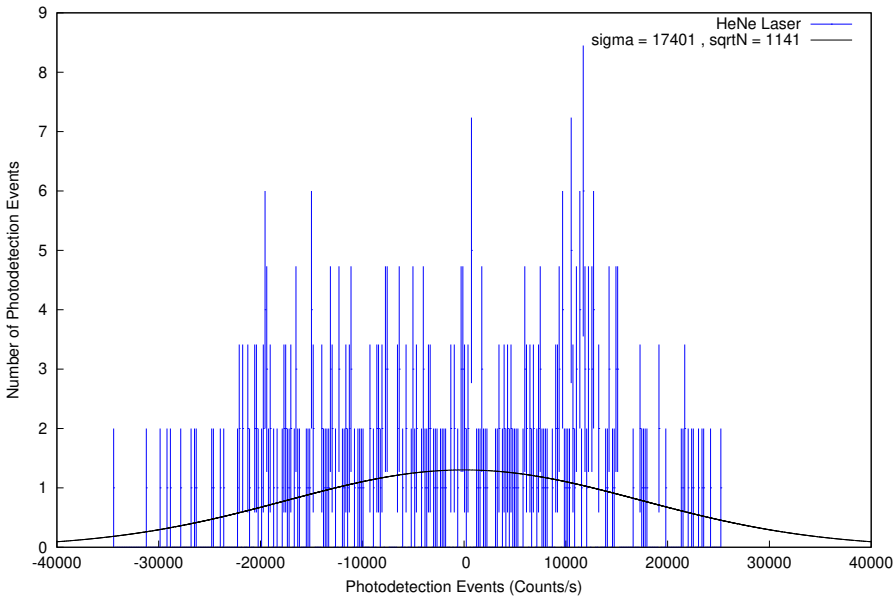

Figure 3.5: Mean: 1302000 ± 2000 counts/s, Standard Deviation σ: 17000 ± 2000 counts/s, $\sqrt{N}$: 1141 counts/s, Gaussian Fit Reduce Chi-Square: 1.00124

Based on the fitted values, the HeNe laser has a percentage noise of about 1.3% and about $15\sqrt{N}$. Additionally, using a power meter, the power output of the laser was measured to be around 3 milliW.

3.2.2 546.1nm Hg Vapour Lamp

We investigated a Hg vapour discharge lamp as it has an atomic emission line at around 546.1 nm, which is close to the 543.5 nm of the HeNe laser. The small difference between the wavelengths reduces the amount of realignment of the interferometer needed when changing between wavelengths.

To determine the emissions lines of the Hg vapour lamp, using a spectrometer, a spectrum of the Hg vapour lamp was measured.

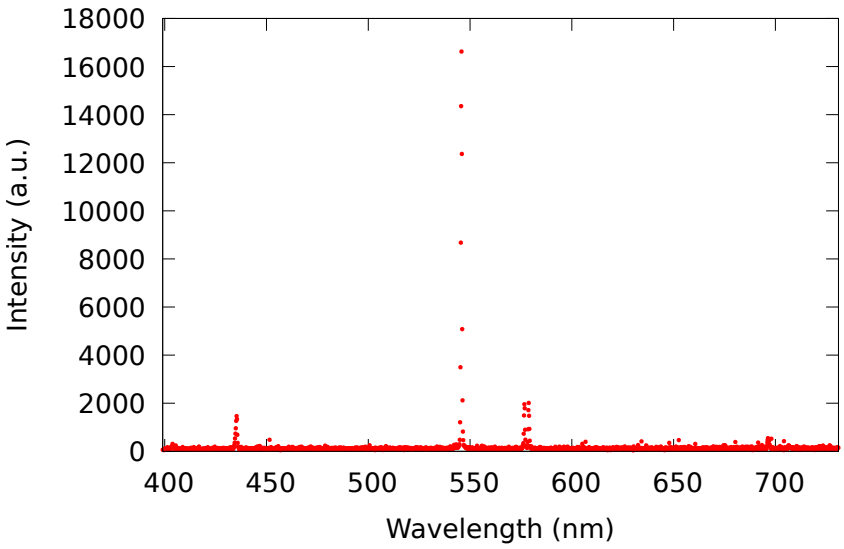

Figure 3.6: Spectrum of Hg vapour lamp measured using a spectrometer. There are multiple peaks which correspond to the various emissions lines of Hg between $399 - 731$ nm.

In our interest at 546.1 nm, a bandpass filter with a centre wavelength of 546 nm and full-width half maximum of 3 nm [17] is used to filter the other emission lines.

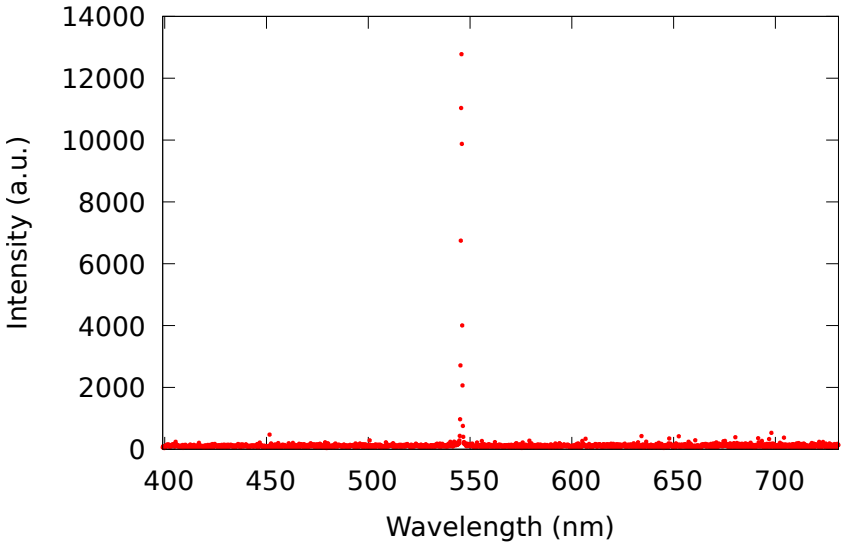

Figure 3.7: The other emission lines are suppressed after filtering with a 546 nm bandpass filter. The dominant peak is now around 550 nm

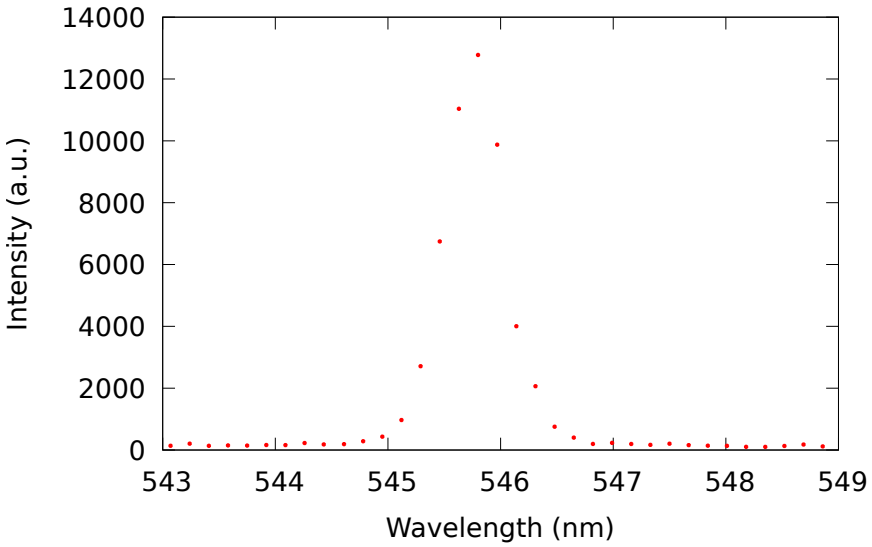

Figure 3.8: The peak dominate emission line after filtering with a bandpass filter is around 546 nm. However, the measurement linewidth is most likely limited by the resolution of the spectrometer.

The spectrum was not fitted to a Gaussian function, unlike the case for HeNe laser, as the measurement is most likely limited by the spectrometer. To approximate the linewidth of the Hg vapour lamp at 546.1 nm, we can approximate using the Doppler broadening of atomic spectral lines [18]

$$\Delta\lambda = \lambda_0 2\sqrt{2\ln 2\frac{kT}{m_0c^2}} \tag{3.12}$$

where, $\Delta\lambda$ is the atomic spectral linewidth, λ_0 is the wavelength when the atoms are at rest, k is the Boltzmann constant, T is the temperature of the atoms, m_0 is the atomic mass, and c is the speed of light.

For Mercury vapour atoms with atomic mass of $3.33 \cdot 10^{-25}$ kg and estimated temperature of 10273 K, and a rest wavelength of 546.1 nm, the wavelength linewidth corresponds to $2.79 \cdot 10^{-3}$ nm. The wavelength linewidth is about 2 orders smaller than the estimated resolution of the spectrometer.

Next, we investigate a Mercury vapour lamp's noise and power output. After coupling the output of a Hg vapour discharge lamp into a single-mode fiber and measured using a single photon detector, the power output is on the order of 10^6 counts/s which corresponds to around 10^{-12} W.

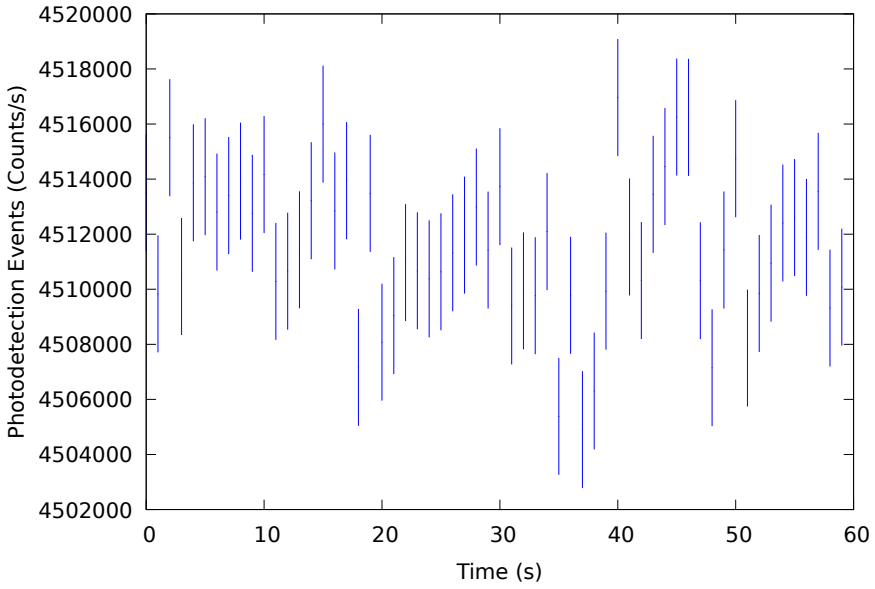

Figure 3.9: A 1 minute measurement of a Hg vapour lamp was measured using a single-photon detector to determine the power output of a single-mode fiber and the amount of noise.

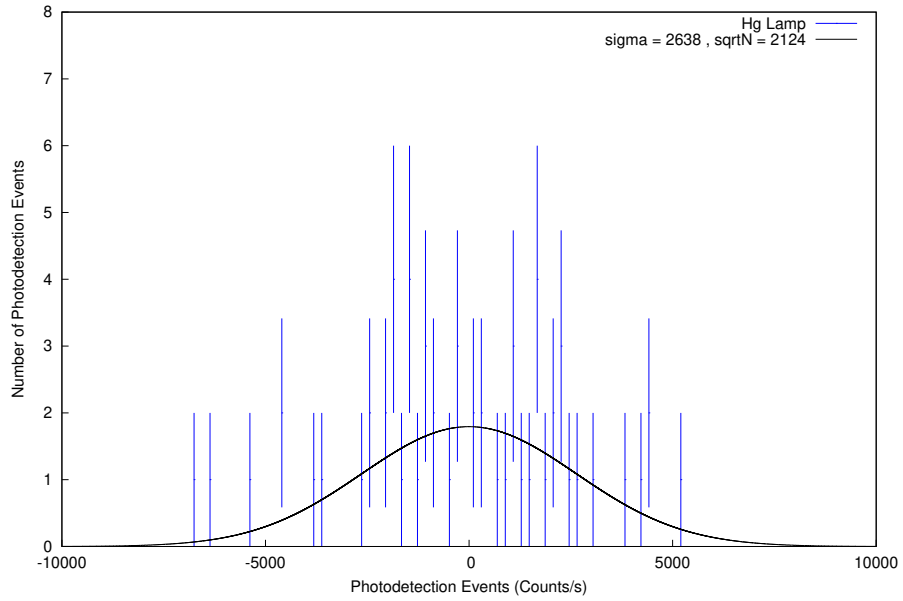

Figure 3.10: Mean: 4511700 ± 400 counts/s, Standard Deviation σ: 2600 ± 500 counts/s, $\sqrt{N}$: 2124 counts/s Gaussian Fit Reduce Chi-Square: 1.00701931

The photodetection events from a 1 minute measurement are binned into bins with width of 196 counts/s and fitted using a Gaussian equation. Using the fitted values, the percentage noise was about 0.5% and was about $1.2\sqrt{N}$.

3.2.3 532nm DPSS Laser

The 532 nm diode-pumped solid-state (DPSS) laser was investigated as a light source as it has a centre wavelength similar to the other two light sources, reducing the amount of interferometer's realignment when switching between wavelengths. It also has a power output on the order of milliwatts, which is about 9 orders brighter than the Hg vapour lamp.

As the HeNe laser has a noise of about $15\sqrt{N}$, we are interested in finding another light source with a smaller noise while having the same order of power output. Hence, we investigated the noise output of the DPSS laser.

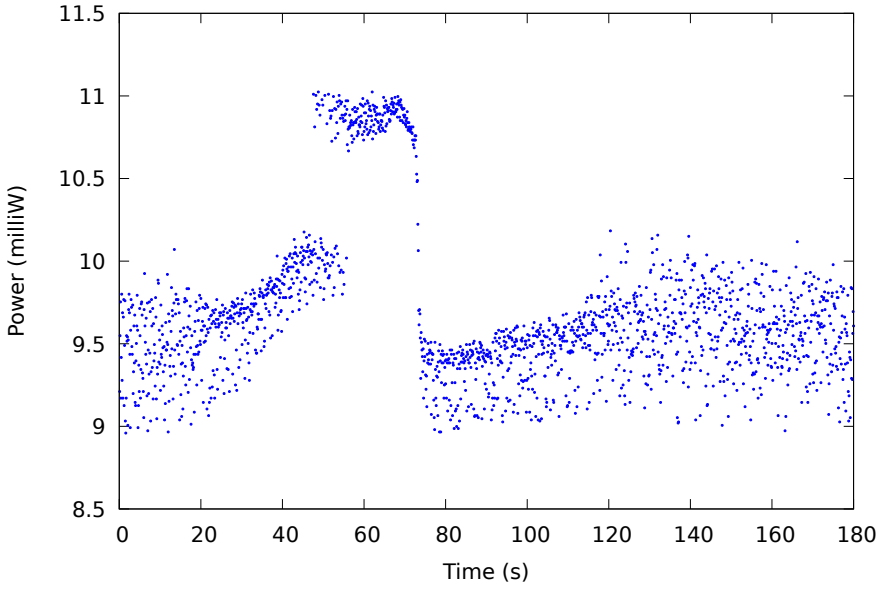

Figure 3.11: For the first 20 s, the maximum power was about 10.1 milliW while the minimum power was about 8.96 milliW, and the average power was about 9.47 milliW.

Taking the differences between the maximum and minimum power and dividing by two for the first 20 s, we get a difference of about 0.56 milliW. By approximating the number of photodetection events for 9.47 milliW, the $\sqrt{N}$ is about $1.6 \cdot 10^8$ counts/s which responds to about $6 \cdot 10^{-8}$ milliW. Therefore, the DPSS laser is about $9 \cdot 10^6 \sqrt{N}$ which is significantly larger than that of HeNe laser. Thus, the DPSS laser was not considered as a replacement for the HeNe laser.

3.3 Conclusion

Light Source	Wavelength (nm)	Power (W)	Noise ($\sqrt{N}$))
HeNe Laser	543.5	$3 \cdot 10^{-3}$	15
Mercury Vapour Lamp	546.1	$1.6 \cdot 10^{-12}$	1.2
DPSS	532	$9.5 \cdot 10^{-3}$	$9 \cdot 10^{6}$

Table 3.1: Table comparing the various light sources. Mercury vapour lamp offer the lowest percentage noise of 0.06%. Power for Mercury vapour lamp are calculated from mean photodetection events of 4511656 c/s

In conclusion, for image inversion interferometry, a light source needs to have a linewidth that gives a temporal coherence length that is longer than the path difference between two beams. A light source also needs to have a small amount of noise, limiting the smallest change in power measurable. It must also have sufficient power to account for coupling loss through the setup.

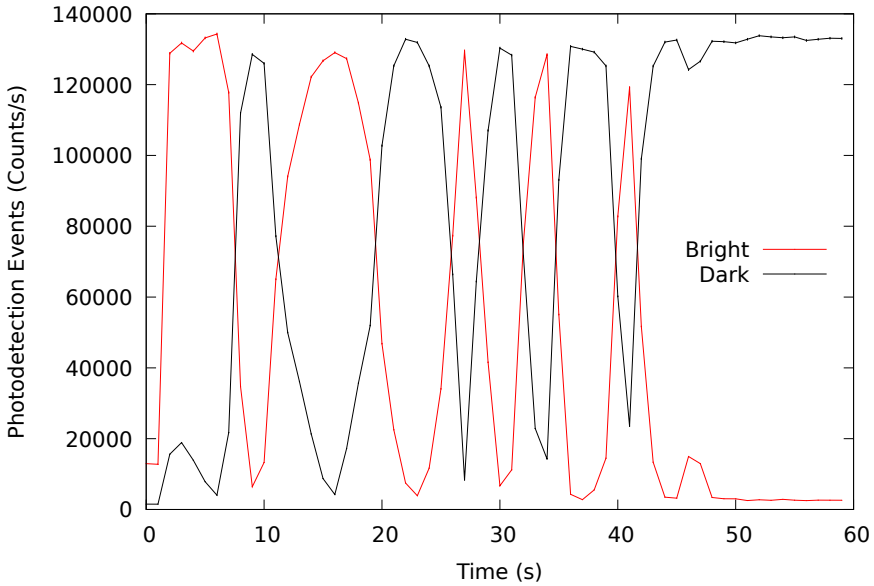

Figure 3.12: When using a HeNe laser, the outputs of a Mach-Zehnder interferometer (Figure 2.1) as the cover slip was rotated. This suggests that interference occurs and the maximum visibility was around 96%.

While the spectrum measurements for the HeNe laser and Hg vapour lamp were potentially spectrometer-limited and require further measurements to determine the linewidths, this may not be a showstopper for now. This is because when using the

HeNe laser as the light source for the Mach-Zehnder interferometer, the outputs of the interferometer suggest that interference occurs in Figure 3.12. Whereas, for the Hg vapour lamp, the temporal coherence length was about 10 cm, which allows for a significant path difference considering the symmetric nature of a Mach-Zehnder interferometer.

While the Hg vapour lamp has the lowest noise compared to the other light sources, its low power output reduces the amount of coupling losses allowed, which is significant in Chapter 6. As such, the HeNe laser was mostly used as the light source for alignment and measurement.

Chapter 4

Generating Radially Asymmetric Light Sources Using Single-Mode Fiber

In this chapter, we investigated various methods to generate radial asymmetric light sources for detection using image inversion interferometry.

To generate radially asymmetric light sources, we begin by considering light sources with radially symmetric intensity distribution functions, such as a Gaussian output from a single-mode fibre. By making use of an opaque obstruction on a radially symmetric light source,

$$I(\bar{r}_{\text{Obstruction}}) \neq I(-\bar{r}_{\text{Obstruction}}) \tag{4.1}$$

where $I(\bar{r}_{\text{Obstruction}})$ refers to the intensity of a point at position vector $\bar{r}$ from the optical axis. When an opaque obstruction partially obstructs a symmetric light source, $I(\bar{r}_{\text{Obstruction}})$ would be 0 while $I(-\bar{r}_{\text{Obstruction}})$ would remain unchanged from a non-zero value.

4.1 Knife Blade

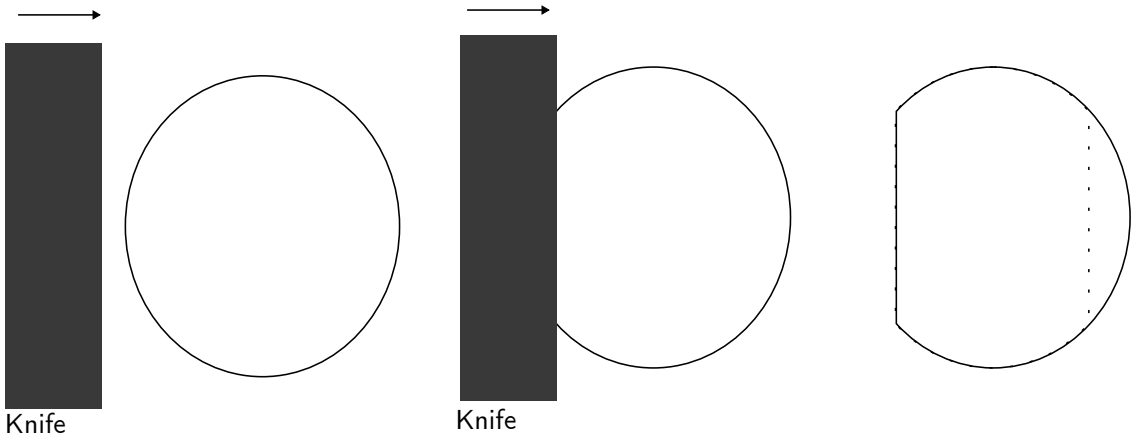

Figure 4.1: LEFT: A knife denoted by a grey rectangle and a radially symmetrical light source denoted by a black circular outline. MIDDLE: A knife partially obstructing a light source. RIGHT: Shape of light source immediately downstream after knife obstruction. Radially symmetrical regions are enclosed by dotted lines.

A knife blade was used as an opaque obstruction to a radially symmetrical light source. As the knife blade translates into the beam, the positions $\bar{r}$ in which intensity goes to 0 increases, increasing regions of asymmetry (regions where the condition Equation 4.1 are satisfied). By measuring power ($P = \int I(\bar{r})d\bar{r}$) downstream from a light source and determining the percentage decrease of in power, we have one method of determining the degree of asymmetry.

4.1.1 Obstruction Percentage

We define obstruction percentage by the percentage decrease in power measured downstream.

$$\text{Obstruction } \% = \frac{P_{\text{No obstruction}} - P_{\text{Obstruction}}}{P_{\text{No obstruction}}} \cdot 100\% \tag{4.2}$$

where $P_{\text{No obstruction}}$ is the power of a light source without a knife obstruction, $P_{\text{obstruction}}$ is the power after a knife is translated.

As such, to control the degree of asymmetry, we attempt to characterise the percentage obstruction for a given knife position. This can be done using a method for knife-edge scanning for beam profiling [19].

A knife is mounted on a linear translation stage such that the knife translates perpendicular to the beam's direction of travel. By measuring the power downstream and fitting it to

$$P(x) = \frac{P_{\max}}{2}\mathrm{erfc}\left(\frac{(x - x_0)\sqrt{2}}{w}\right) + P_{\text{offset}} \tag{4.3}$$

where $P(x)$ is the power measured, $P_{\max}$ is the maximum power without knife obstruction, $\mathrm{erfc}(\dots)$ is the error function, x is the knife position on the linear translation stage, x_0 is the mean knife position, w is the beam radius, and P_{offset} is the power offset when fitting. The fitted parameters give us a means to determine $P(x)$ for each knife position.

4.1.2 Characterising a collimated beam

We first performed a knife-edge measurement on a collimated beam to familiarise with the knife-edge beam profiling method.

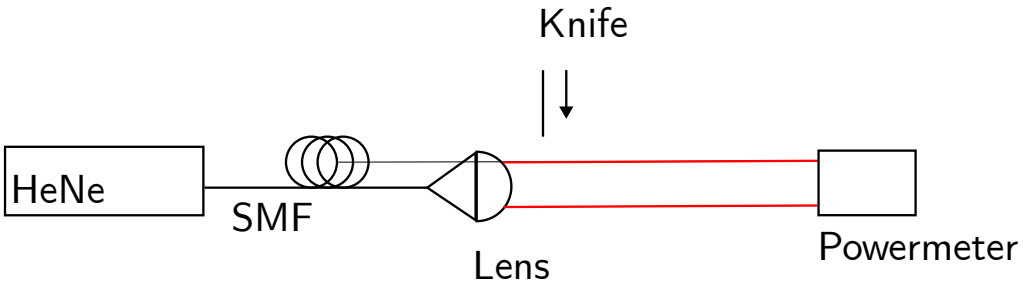

Figure 4.2: Experimental setup for a knife edge measurement on a collimated beam.

Light from a HeNe laser was coupled into a single-mode fibre before being collimated using an aspheric lens. A knife was mounted on a linear translation with a stepper motor and was placed downstream from the lens. The power was measured with a Si-based power meter.

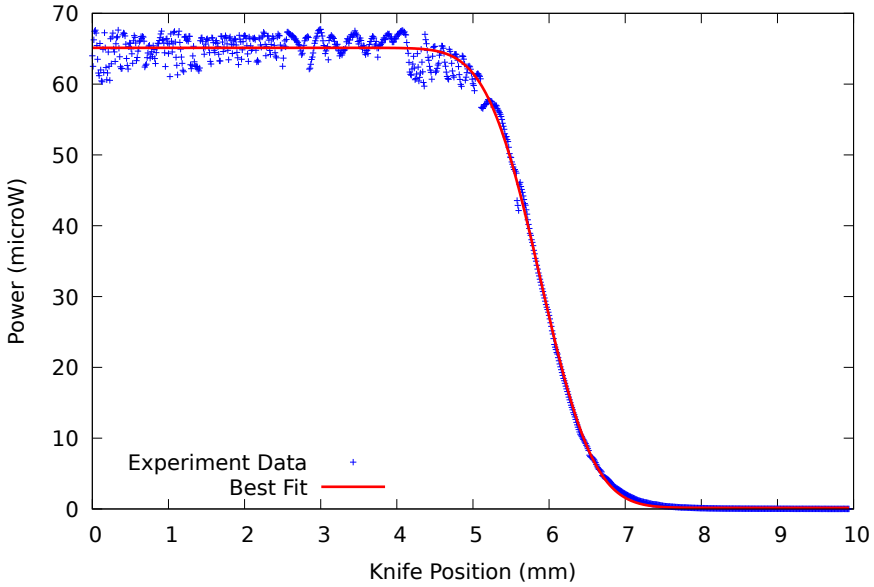

Figure 4.3: Knife Edge measurement on a collimated beam. The fitted parameters are reduced chi-square: $1.7 \cdot 10^{-12}$, P_{offset}: $(1.6 \pm 0.8) \cdot 10^{-7}$ W, P_{max}: $(6.50 \pm 0.01) \cdot 10^{-5}$ W, x_0: $(5.883 \pm 0.003) \cdot 10^{-3}$ m, and w: $(1.108 \pm 0.009) \cdot 10^{-3}$ m

The aspheric lens used was for a ThorLabs F220FC-A, which claims to collimate a beam waist to 2 mm [20]. The beam waist differs from the beam waist calculated from knife edge measurements ($2w = 2.2$ mm). This could be due to the difference in fiber type used to project the light on the lens.

4.1.3 Bare Single-Mode Fiber

In our subsequent experiment setups in Chapter 6 and Chapter 7, we made use of a bare single-mode fiber to generate a point light source. With the above insights, we characterised the obstruction percentage of a knife obstructing the output of a bare single-mode fiber.

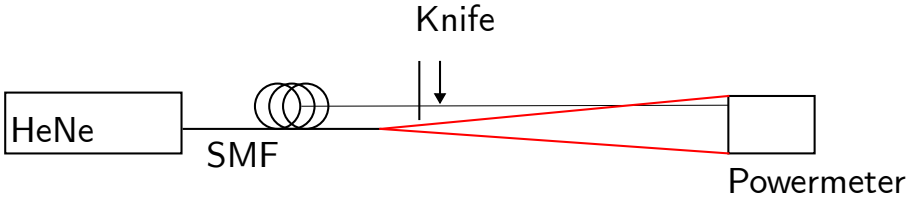

Figure 4.4: Experimental setup of a knife-edge measurement on a diverging beam from a bare single-mode fiber. The knife was mounted as close to the bare fibre tip as possible to reduce the beam diameter at the plane where the knife obstructs.

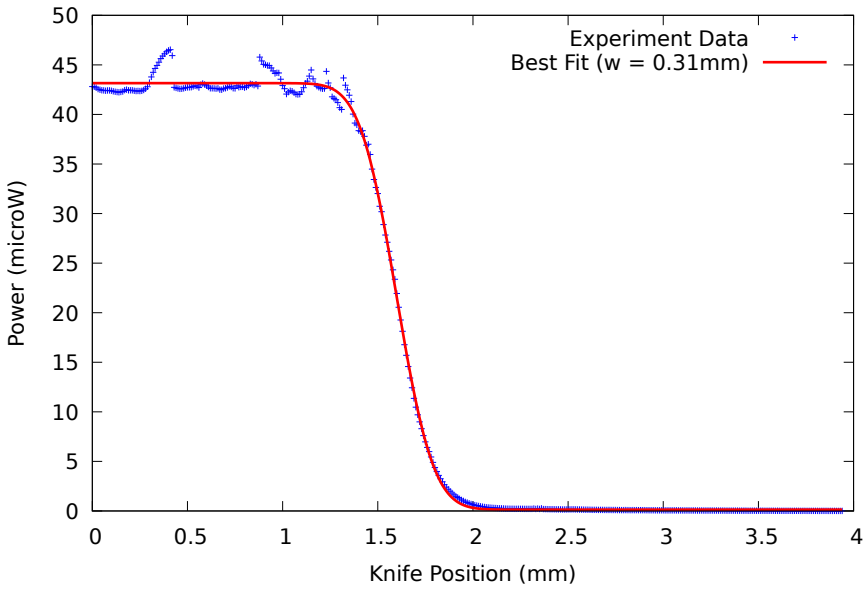

Figure 4.5: Knife Edge measurement of a diverging beam after SMF. Reduced chi-square: $1.7307 \cdot 10^{-10}$, P_{offset}: $(1.3 \pm 0.5) \cdot 10^{-7}$ W , P_{max}: $(4.302 \pm 0.008) \cdot 10^{-5}$ W, x_0: $(1.599 \pm 0.001) \cdot 10^{-3}$ m, and w: $(3.05 \pm 0.03) \cdot 10^{-4}$ m

The beam waist ($2w$) at which the knife obstructs the beam is therefore $(6.10 \pm 0.07) \cdot 10^{-4}$ m. This method gives a way to quantify the diameter of the source in Chapter 6.

In image inversion interferometry, with only access to the image plane, we attempt to characterise the percentage obstruction against knife position.

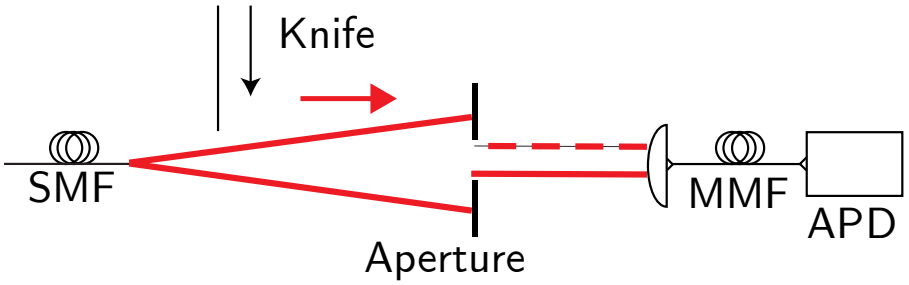

Figure 4.6: Schematic showing experiment setup characterising knife position by measuring the intensity after an aperture. For simplicity, a lens focusing light into a multi-mode fiber (MMF) that is connected to an avalanche photodiode (APD) is shown after the aperture. However, in the actual setup, light passes through a Mach-Zehnder interferometer with image inversion lenses in Figure 6.3. The photodetection events from the two outputs are added together to represent the output after the aperture.

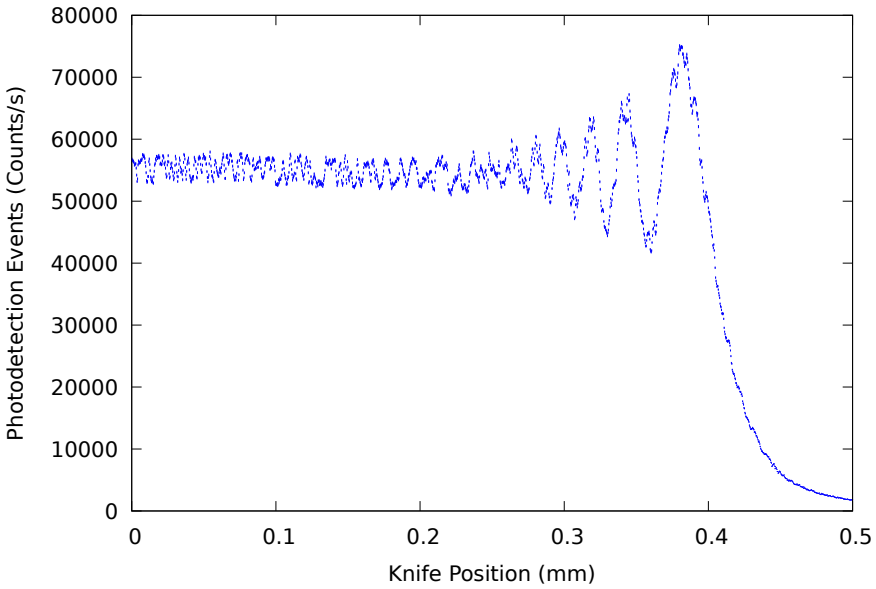

Figure 4.7: Intensity measured downstream from a knife and through an aperture diameter of 1.6 mm positioned about 1 m away.

The intensity against the knife position is presented. Using the first 0.05 mm, we can estimate the minimum percentage obstruction resolvable from half the difference of the maximum value (58458 counts/s) and minimum value (52149 counts/s). This gives 3155 counts/s which is about 5.6%. Since the difference is about $15\sqrt{N}$, it suggests that the oscillations are contributed by the HeNe laser used.

4.2 Thin Strips

A knife blade increases in obstruction percentage as the knife is translated into the beam until the entire beam is fully obstructed. However, this may not apply in physical situations where the maximum percentage obstruction is less than 50%

Using thin strips of objects with smaller diameters than the incoming beams would ensure that the maximum percentage obstruction would always be less than 100%.

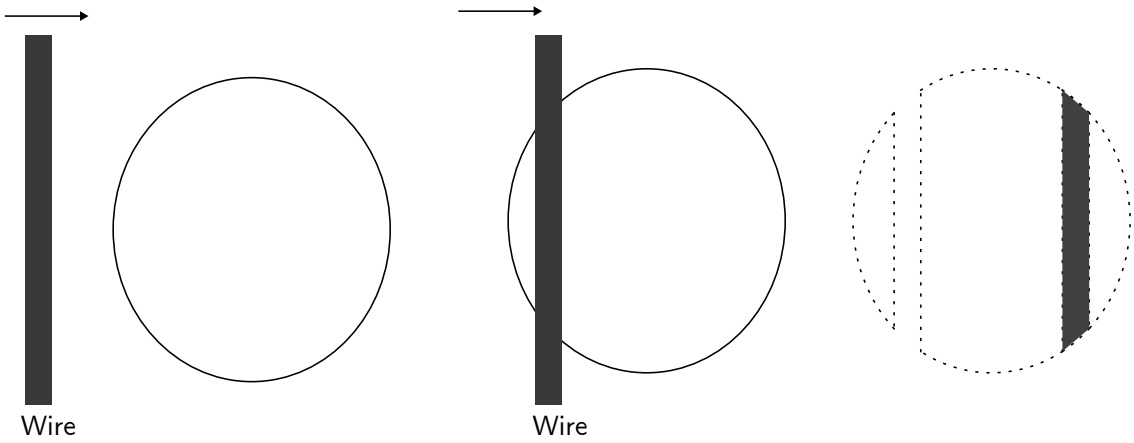

Figure 4.8: LEFT: A piece of wire denoted by a grey rectangle and a radially symmetrical light source denoted by a black circular outline. MIDDLE: A piece of wire partially obstructing a light source. RIGHT: Shape of light source immediately downstream after knife obstruction. Radially symmetrical regions are enclosed by dotted lines, while asymmetrical regions are denoted by grey.

4.3 Conclusion

In conclusion, to generate radially asymmetric light sources, we choose to generate radial asymmetries through the use of an opaque obstruction. In an attempt to quantify the degree of asymmetry, we measure the change in power received after the obstruction.

As such, the smallest measurable obstruction percentage would be limited by the power and noise of the light source and, in this case of Figure 4.7, the HeNe laser. While using the Hg vapour lamp would be a better option considering the $1.2\sqrt{N}$, it was not viable due to coupling losses through the distance of 1 m and aperture diameter of 1.6 mm

However, using a change in power to quantify the degree of asymmetry assumes that the power distribution across the beam is uniform, which may not be the case for the output of a single-mode fiber. Moreover, it may only work for obstructions that increase in obstruction area from the edge of the beam. This may not work for certain obstructions, such as thin strips. When the percentage obstruction of thin strips is at the maximum, the degree of asymmetry also depends on the position of the thin trip across the beam. Further analysis will be required to properly define the degree of asymmetry.

Chapter 5

Radial Asymmetries At The Pupil Plane

In this chapter, we attempted to detect radial asymmetric light sources at the pupil plane using image inversion interferometry. The pupil plane of an imaging system refers to the aperture of an optical system. This was an attempt to replicate and build upon what was previously done in the research group [21, 22].

5.1 Experimental Setup

Using methods discussed in Chapter 4 to generate radial asymmetric light sources at the pupil plane, we present a method as a proof-of-concept to detect radial asymmetric light sources using image inversion interferometry.

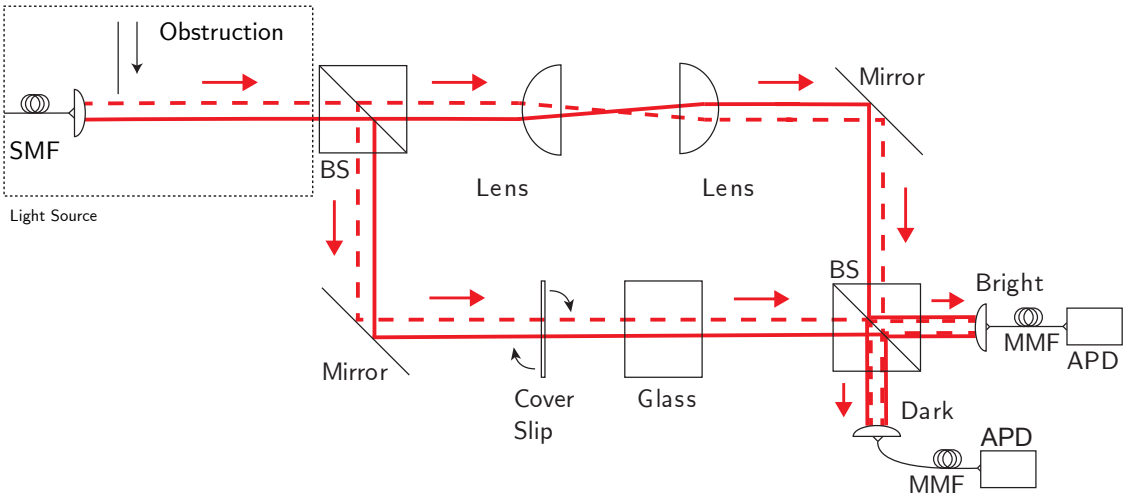

Figure 5.1: Experimental setup for the detection of radial asymmetric light sources at the pupil plane. The radially asymmetric light source refers to the portion enclosed in the dotted box. The pupil plane refers to the entrance of the first beamsplitter.

The experimental setup for image inversion interferometry is a Mach-Zehnder interferometer with a pair of lenses inserted into one of the beams [9, 13, 21, 22].

For the generation of a radial asymmetric light source, light from a HeNe laser ($\lambda = 543.5\,\text{nm}$) is coupled into a single-mode fibre such that it is projected into TEM_{00} fundamental mode for spatial coherence and radial symmetry. The light is then collimated into a beam with a waist diameter of around $2 \cdot 10^{-3}\,\text{m}$. An obstruction mounted on a linear translation stage is then allowed to translate at normal incident into the direction of the beam.

For image inversion interferometry, the light from an asymmetric light source is separated using a 50:50 non-polarising beamsplitter (BS). The transmitted beam passed through a pair of achromatic plano-convex doublet lenses ($f = 19\,\text{mm}$, thickness, $d = 6\,\text{mm}$) that are positioned in a telescope configuration with unity magnification. This pair of lenses are referred to as image inversion lenses. The reflected beam passed through a glass block ($d = 12.7\,\text{mm}$) and a thin piece of glass ($d = 170$ microns) mounted on a rotation stage. The transmitted and reflected beams meet and interfere at another 50:50 non-polarising beamsplitter. The two outputs, dark and bright, of the interferometer are then each coupled into a multi-mode fibre connected to an avalanche photodiode (APD). The photodetection events were timestamped at 2 ns resolution.

To maximise interferometric visibility, a linear polariser was added upstream from the obstruction to filter vertically polarised light as orthogonal polarised light does not interfere with each other. Moreover, a glass block in the reflected beams compensates for the increase in path length due to the image inversion lens such that the path differences are within the light source temporal coherence length.

5.2 Gain in Signal-to-Noise Ratio

We attempt to quantify whether image inversion interferometry has any benefits over direct measurement methods. One way to do this is to compare the signal-to-noise ratio of both methods.

To define the signal-to-noise ratio, consider the interferometric visibility of an interferometer and the input intensity on the interferometer. The intensity for the dark output can be calculated.

$$I_{\text{Dark}} = \frac{I_0}{1 + \frac{1+V}{1-V}} \tag{5.1}$$

where I_{Dark} is the intensity of the dark output, I_0 is the input intensity, and V is the interferometric visibility. If we generate a radial asymmetric light source using an obstruction of a light source, we can quantify the degree of asymmetry using obstruction percentage, $x\%$.

$$I_{\text{Dark Inversion}} = I_{\text{Dark}} + \frac{1}{2} \cdot \frac{x}{100} I_0 \tag{5.2}$$

The signal-to-noise ratio of radial asymmetry in the dark fringe can be defined as follows

$$\text{SNR}_{\text{dark}} = \frac{I_{\text{Dark Inversion}} - I_{\text{Dark}}}{\sqrt{I_{\text{Dark Inversion}}}} \tag{5.3}$$

The signal-to-noise ratio of radial asymmetry for direct measurement is

$$\text{SNR}_{\text{Total}} = \frac{\frac{x}{100} I_0}{\sqrt{I_0 - \frac{x}{100} I_0}} \tag{5.4}$$

However, for this model to be valid, it assumes that the intensity across the beam of a light source is uniform. Moreover, only a single point on the beam is obstructed. As such, the maximum percentage obstruction is 50%, beyond which the model fails. Moreover, it also assumes that the contribution of noise is modelled after Poissonian distribution.

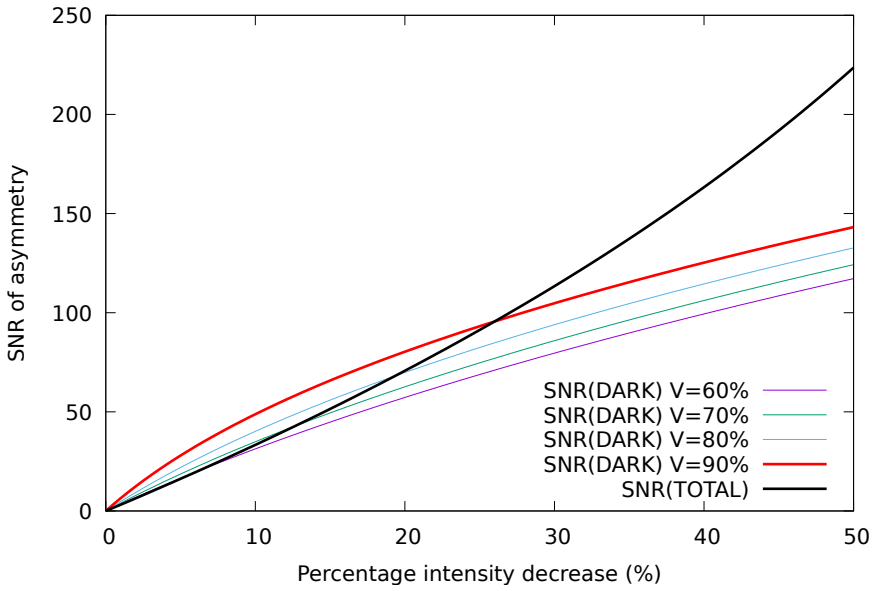

Figure 5.2: Plot of a calculated signal-to-noise ratio of asymmetries using image inversion (dark) and direct measurement (total) for various interferometric visibility.

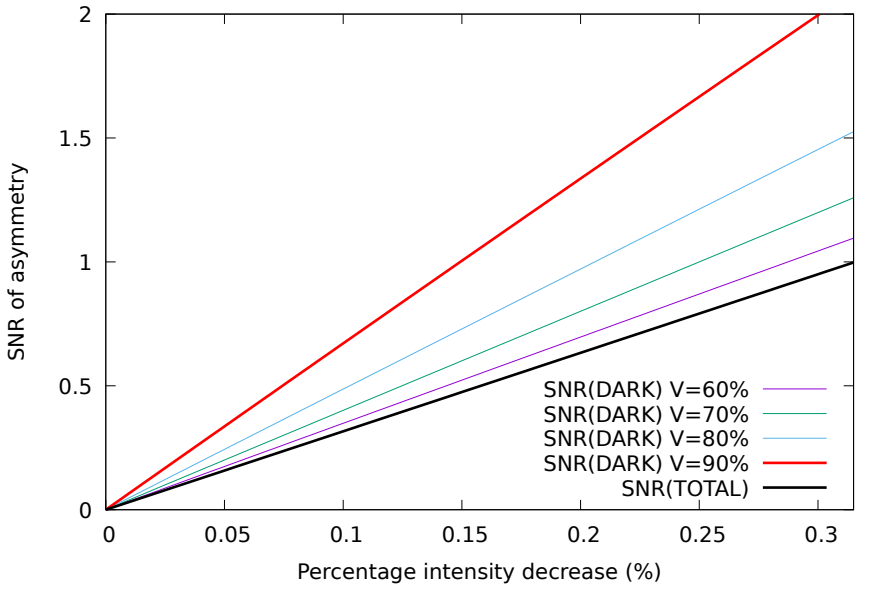

Figure 5.3: There is region of percentage obstruction where SNR of direct measurement (total) is less than one but SNR of dark output is more than 1.

This shows that the largest percentage obstruction such that image inversion has a higher SNR compared to direct imaging is limited by the visibility of the interferometer.

5.3 Measuring Radial Asymmetries

In this section, we translated various obstructions across the beam to generate radial asymmetric light sources and compared the signal-to-noise ratio of asymmetry. Direct measurement refers to the sum of the interferometer's dark and bright outputs denoted by total.

To compute the signal-to-noise ratio from a measurement,

$$\mathrm{SNR}_{\mathrm{Total}} = \frac{I_{\mathrm{Total}} - I_{\mathrm{Total\ Reference}}}{\sqrt{I_{\mathrm{Total}}}} \tag{5.5}$$

$$\mathrm{SNR}_{\mathrm{Dark}} = \frac{I_{\mathrm{Dark}} - I_{\mathrm{Dark\ Reference}}}{\sqrt{I_{\mathrm{Dark}}}} \tag{5.6}$$

5.3.1 Thin Strips

A wire with a diameter of 0.7 mm was used as an obstruction and was translated into a radially symmetrical beam to generate radial asymmetry.

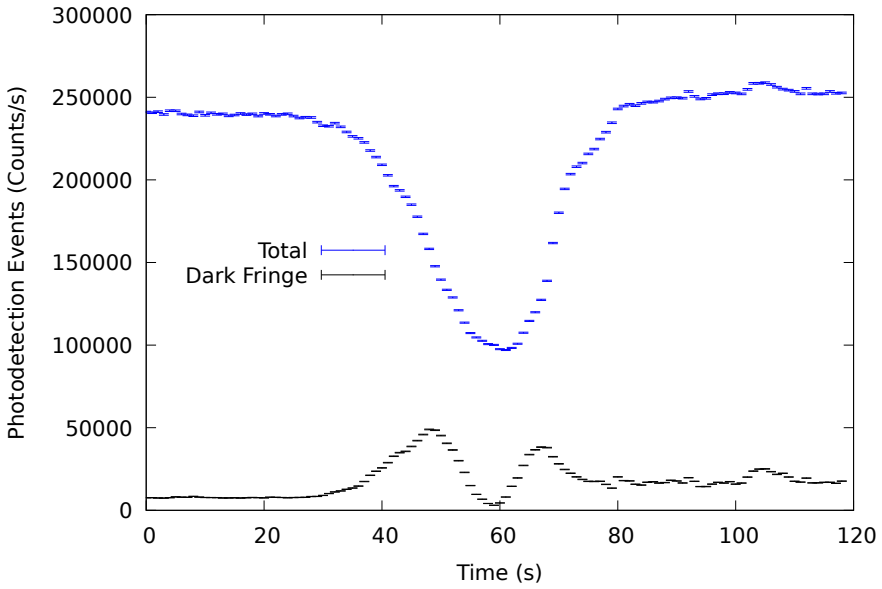

Figure 5.4: A wire with a diameter of 0.7 mm was translated into the beam to generate a radial asymmetry light source. At the 0th second, the interferometric visibility was 94%.

As a wire was translated into the laser beam, the reduction in photodetection events of total suggests that the wire has started obstructing a light source. For total, the minimum photodetection events occurred at the 62$^{\mathrm{nd}}$ second with a

photodetection events of 97018 counts/s. By comparing the photodetection event at 0^{th} second, the maximum percentage obstruction is about 60%.

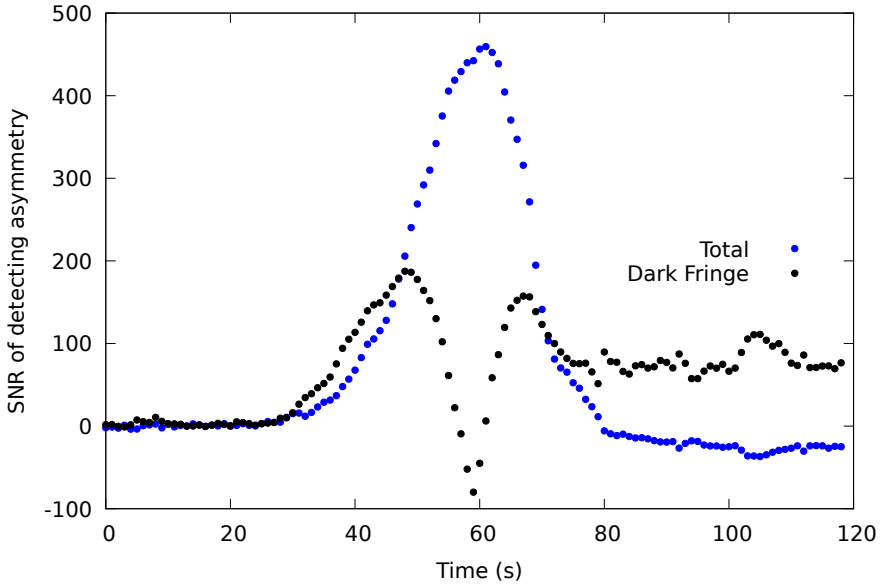

Figure 5.5: Computed SNR of asymmetry for both dark and total. The photodetection events at the 0^{th} second for used as reference. For total, the reference was 240093 counts/s, while the reference for dark fringe: 7481 counts/s.

As the wire was translated into the beam, the percentage obstruction increased to a maximum of 60%. From Figure 5.5, there the regions which have SNR of dark greater than total are around 30^{th} second to around 50^{th} second. While for regions around 70^{th} seconds and above, the SNR for dark fringe is greater than total, the higher photodetection events for regions above 70^{th} seconds than those before 30^{th} seconds in Figure 5.4 suggests that other factors may have contributed to the increase in SNR. A higher photodetection event above reference for regions above 70^{th} contributed to the negative SNR values.

Using the photodetection event from the last bin in the measurement, the visibility was 86%. This suggests that visibility has changed from the initial value of 94%.

5.3.2 Knife

A knife that was mounted on a linear translation was used as an obstruction.

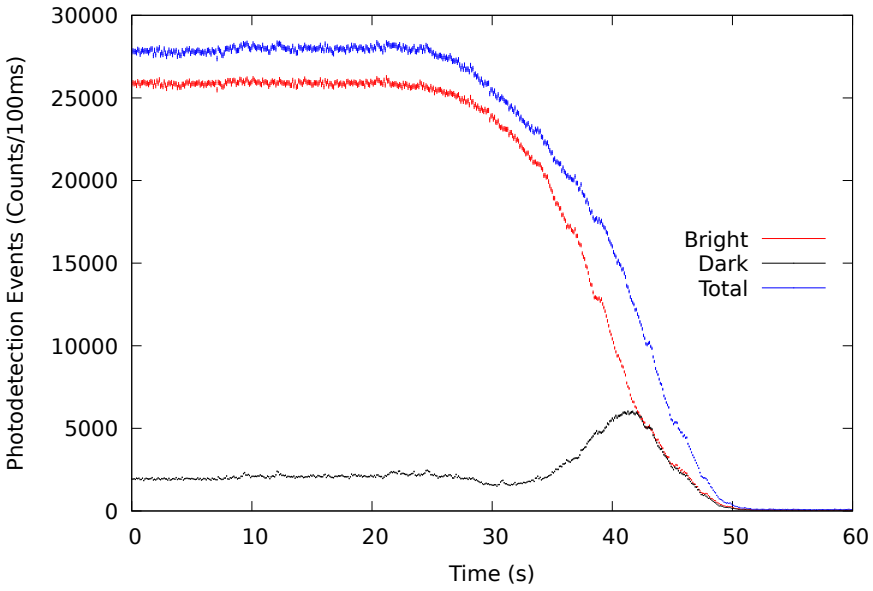

Figure 5.6: A knife was translated into the beam to generate a radial asymmetric light source and measured using image inversion interferometry. The interferometric visibility at the 0^{th} second was 86%

As the knife is translated into the beam, the percentage obstruction increases. The 50% percentage obstruction occurs around 41^{th} second. Above a percentage obstruction above 50%, the two paths of the Mach-Zehdner interferometer do not overlap and thus split equally in the bright and the dark output. This could explain why the bright and dark outputs have similar photodetection events above 40^{th} second.

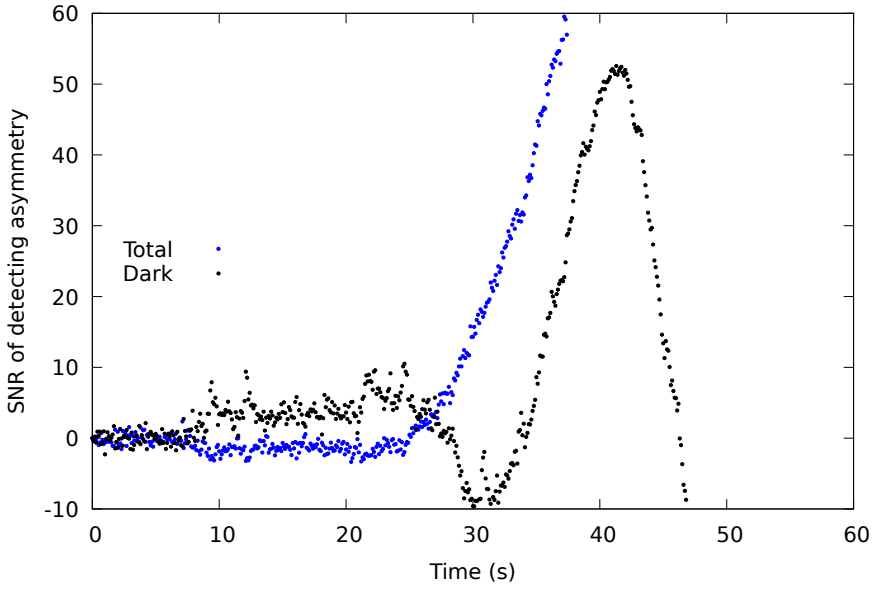

Figure 5.7: Computed SNR of asymmetry for dark and total. Reference for total was 27771 counts/100ms and reference for dark was 1939 counts/100ms

At around 25$^{\text{th}}$ second, there is a small region in which the SNR of dark is higher than the SNR of total. The percentage obstruction ranged from 0.3% to 1.3%, which suggests that they are within the percentage noise of the laser. This is because approximating a noise of $\sqrt{N} = 167$ counts/100ms for HeNe laser, the percentage noise is about 0.6%, suggesting that percentage obstruction was not due to the obstruction but laser noise.

5.4 Conclusion

In conclusion, we used percentage obstruction as one metric to quantify the degree of asymmetry. Hence, to show a regime in which image inversion's SNR is better than direct measurement, we will need to control a few parameters.

Since the smallest percentage obstruction depends on the noise of the light source, these measurements should have been taken with a Hg vapour lamp instead of the HeNe laser. The Hg vapour lamp has a lower amount of noise compared to the HeNe laser.

A stepper motor should have been used to translate the obstruction into the beam to better control the obstruction percentage. The step sizes of 0.0003125 /step allow for finer resolution than a standard micrometre screwgauge

Measurements should also be taken against the obstruction position instead of in time to know the percentage obstruction at each position for repeatability.

Lastly, visibility stability should have been quantified so that we can determine the drift of visibility, which affects the measurements' SNR.

Chapter 6

Radial Asymmetry at Object Plane

In Chapter 5, radial asymmetry was generated at the pupil plane instead of the object plane of an imaging system. This could be similar to imaging a dust particle between an optical lens and the CMOS sensor of a camera instead of imaging a dust particle at a distance from the lens. Hence, we present a proof-of-concept experiment to investigate radial asymmetry at the object plane.

6.1 Experimental Setup

6.1.1 Radial Asymmetric Light Source

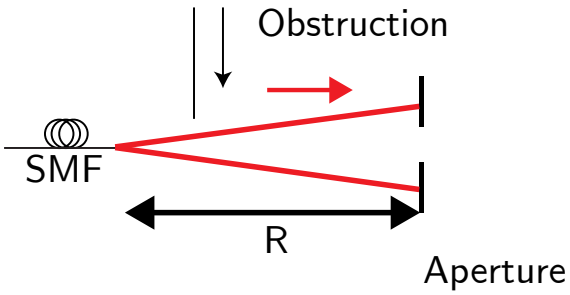

Figure 6.1: Schematic showing the generation of a radially asymmetric light source before an aperture. Light from a single-mode fiber (SMF) is partially obstructed by using an obstruction to generate radial asymmetries. An iris with a variable diameter is used as an aperture of the imaging system.

As we assume that the radial asymmetries we are investigating have small angular diameters with respect to the aperture, the diameter of a radial asymmetric light source could be approximated using the equation for the arc length of a circle,

$$s = R\theta \tag{6.1}$$

where s is the diameter of a radial asymmetric light source, R is the distance between the radial asymmetric light source and the aperture, and θ is the minimum resolvable angular separation at the obstruction's plane given by Rayleigh's criterion.

By substituting the Rayleigh criterion for circular aperture [1],

$$s = R \sin^{-1} 1.22 \frac{\lambda}{D} \tag{6.2}$$

a relationship between the diameter of a radial asymmetric light source s, the distance between a radial asymmetric light source and aperture R and the diameter of the aperture D is formed for a fixed wavelength λ of a light source.

To minimise the beam diameter of a radial asymmetric light source, the obstruction will be mounted as close to the fiber tip as possible. As such, based on knife edge measurements in Chapter 4, we approximate the beam diameters to be on the order of 10^{-4} m. Thus, fixing the beam diameter of a radial asymmetric light source.

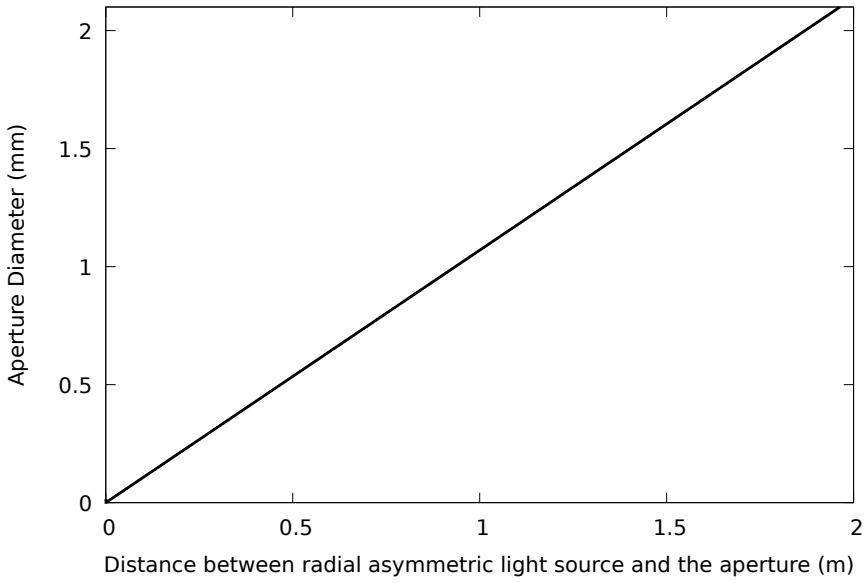

Figure 6.2: For wavelength (λ) of light is 543.5 nm and the diameter of a radial asymmetric light source (s) is $6.2 \cdot 10^{-4}$ m.

6.1.2 Coupling Loss

The consideration for the choice of distance R and aperture diameter D could affect the losses in power received after the aperture. Loses could result from the aperture having a smaller area than the beam diameter of a radially asymmetric light source at the aperture.

To give an approximation for the amount of power loss, we first consider an approximation of beam divergence from a fiber using

$$D_{\text{Fiber}} = 2NA * R \tag{6.3}$$

where D_{Fiber} is the diameter of a radially asymmetric light source at a distance R from the tip of a single-mode fiber. NA is the numerical aperture of the fiber,

To approximate the amount of power loss, we compare the area of the aperture and the beam diameter of a radially asymmetric light source at the aperture's plane.

$$P_{\text{After aperture}} = P_{\text{At fiber}} \frac{\pi(D/2)^2}{\pi(D_{\text{Fiber}}/2)^2} \tag{6.4}$$

where, $P_{\text{After aperture}}$ is the power measured after the aperture and $P_{\text{At fiber}}$ is the power measured at aperture. Thus, coupling losses can be approximated using,

$$\text{Coupling} \approx \left(\frac{D}{D_{\text{Fiber}}}\right)^2 \tag{6.5}$$

For a distance R of 1 m and iris diameter D of 1 mm, the coupling losses is about 10^5 orders.

6.1.3 Image Inversion Interferometry

The experimental setup for image inversion interferometry was similar to Chapter 5 with the addition of an iris as an aperture that could vary the beam diameter before the first beamsplitter.

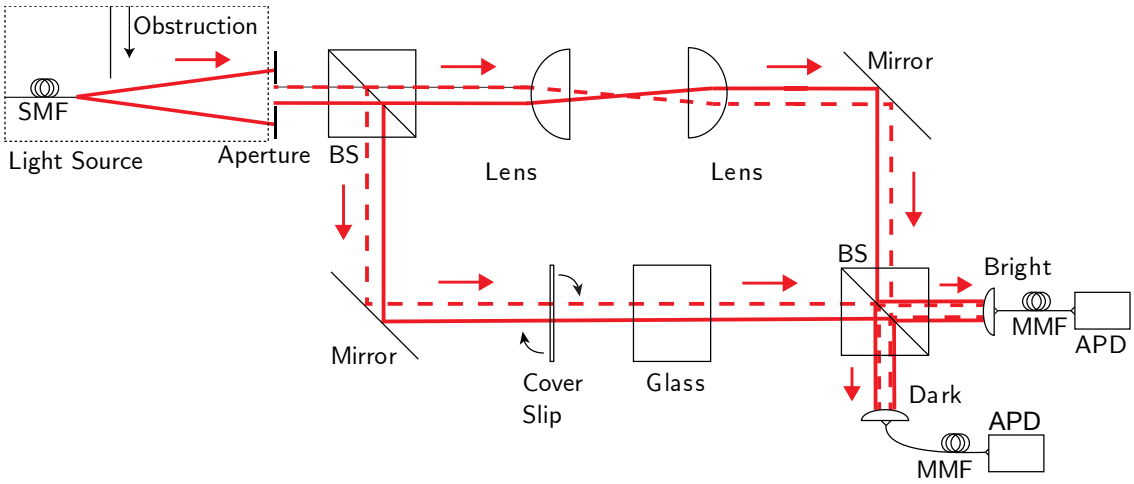

Figure 6.3: Schematic of experiment setup to investigate radial asymmetry at the object plane. The generation of a radially asymmetric light source (in a dotted box) is before the aperture. The aperture acts as the pupil plane for the image inversion interferometry.

For the light source, light from a HeNe laser is projected into a single-mode fiber for spatial coherence and symmetry before being allowed to diverge at the end of the fiber. An obstruction mounted on a linear translation stage allows an obstruction to be translated into the beam. To minimise the beam diameter at the obstruction plane, the obstruction is mounted as close to the fiber tip as possible ($\approx 1\,\text{mm}$ between fiber tip and obstruction). There is a distance of about 1 m between the obstruction plane and the iris.

For image inversion interferometry, diverging light passes through an iris, acting as an aperture. The iris diameter could be varied from 1 mm to 12 mm. The iris diameter is determined by the distance between the obstruction plane and the iris using the relationship in Figure 6.2. The output after an iris is sent into a Mach-Zehnder interferometer that has a similar configuration to the setup in Chapter 5.

6.2 Experimental Results

6.2.1 Measuring Iris Diameter

To determine the iris diameter, we attempted to take an image of the iris.

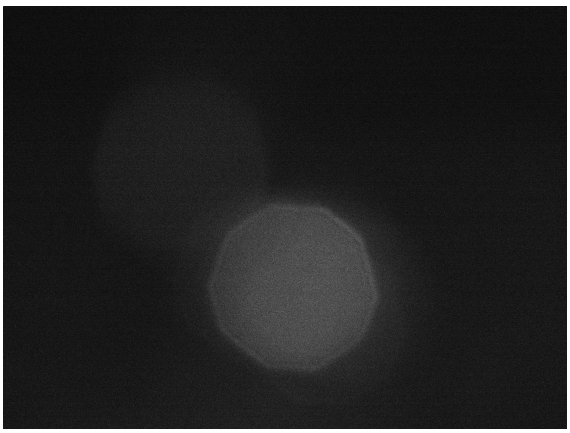

Figure 6.4: A camera was placed at the opening of the iris such that ambient light passing through the iris could be imaged. This allows us to quantify the iris diameter.

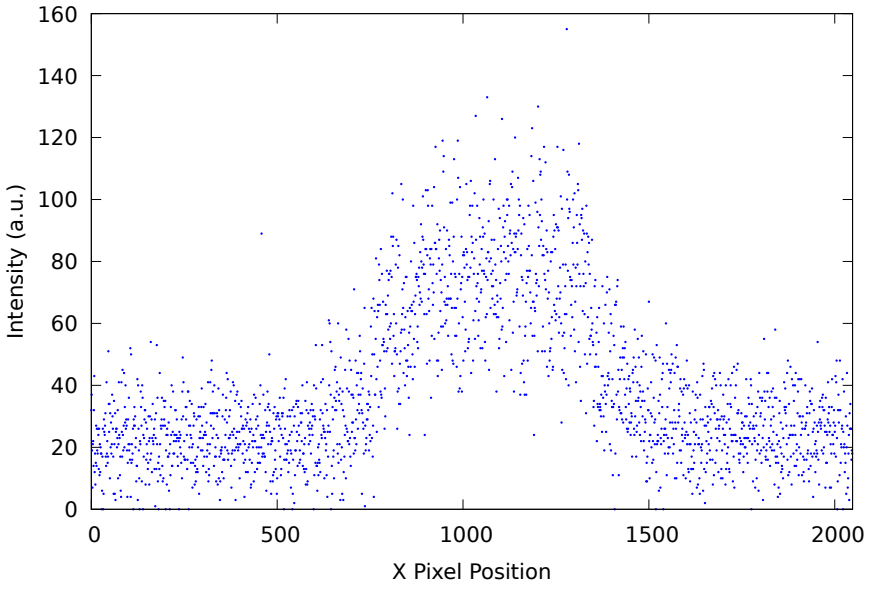

Figure 6.5: Pixel intensities for row 1100. There are 454 pixels above the pixel intensity of 60.

There are 454 pixels above the arbitrarily determined threshold value of 60. Using pixel size of $3.45 \cdot 10^{-6}$m [23], the iris diameter is about 1.6 mm.

Using Figure 6.2, the iris diameter for 1 m distance between fiber and iris is about 1 mm. As such, the radial asymmetric light source may not have been diffraction-limited with respect to the iris and could not be considered a point source.

However, this isn't a showstopper, as the original intention for diffraction-limited

was for a spatially coherent beam after the iris. However, since a single-mode fiber is used, the beam is already spatially coherent.

6.2.2 Measuring asymmetries

Similar to the situation in the near-field, we investigated using percentage obstruction as a metric for the degree of asymmetries.

A knife mounted on a linear translation stage with a steppermotor was used as an obstruction to generate a radial asymmetric light source.

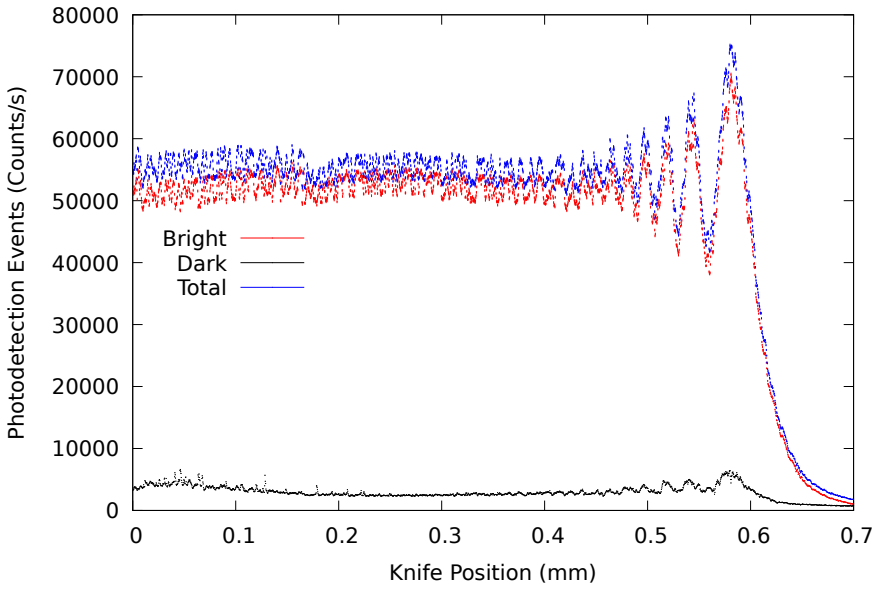

Figure 6.6: The knife was translated at 0.0003125 mm/step. The interferometric visibility at the 0 mm position is 88%.

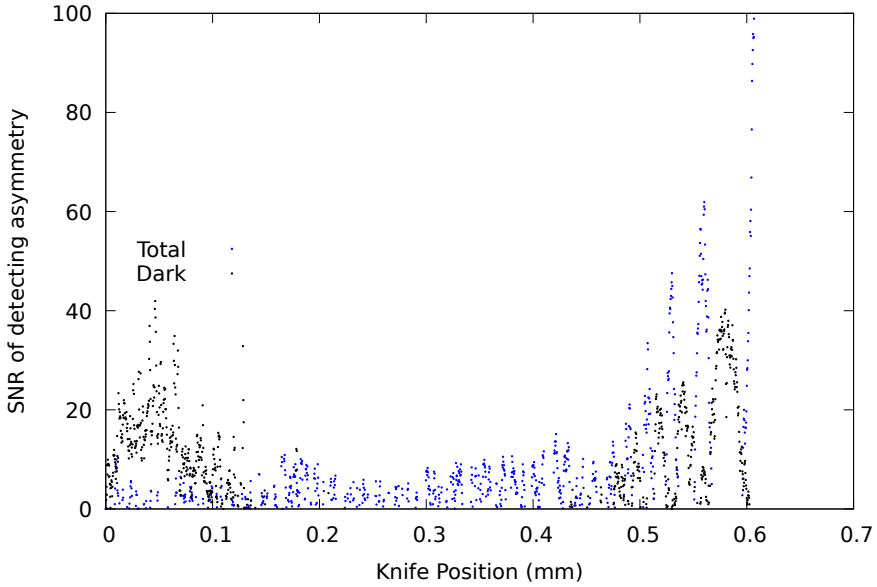

Figure 6.7: The SNR for total and dark was computed using Equation 5.5 and Equation 5.6 respectively. The reference for total was 54425 counts/s, while the reference for dark was 3202 counts/s

As the knife is translated into the beam, there seem to be increasing oscillation patterns. As this is the same data as Figure 4.7, we estimated that the minimum percentage obstruction resolvable is about 5.6%. Since the difference was about $15\sqrt{N}$, it suggests that the oscillations are contributed by the HeNe laser used.

6.3 Conclusion

In conclusion, there doesn't seem to be an increase in SNR for the direct measurement (total) case compared to the SNR (dark). This could be due to the stability of the HeNe laser.

Switching the HeNe laser to Hg was not possible due to the 10^5 coupling losses between the single-mode fiber and after the iris.

The increasing oscillations may be the result of knife-edge diffraction. However, more investigation will be needed to quantify whether it is indeed knife-edge diffraction.

As a mistake was made in determining the iris diameter, the light source may not be diffraction-limited. As such, a follow-up measurement would be required to investigate the radial asymmetries of a point light source.

Chapter 7

Direct Measurement of Radial Asymmetric Point Light Sources

In this chapter, we investigate various methods of direct measurement. The common method used in the previous section to quantify direct measurement considers the total intensity received after the iris. However, the two-dimensional spatial information is then lost.

7.1 Fraunhofer Diffraction

Consider light at wavelength λ emitted in all directions from a point source (Point P). The emitted wavefront encompasses a spherical shape. When the spherical wavefront produced by the point source reaches a slit, it undergoes diffraction. The diffraction pattern can be approximated using either Fresnel Diffraction or Fraunhofer Diffraction. Fresnel Diffraction considers the near-field regime where spherical waves undergo diffraction, while Fraunhofer diffraction considers the far-field regime where incoming waves on the slit are planar. [12]

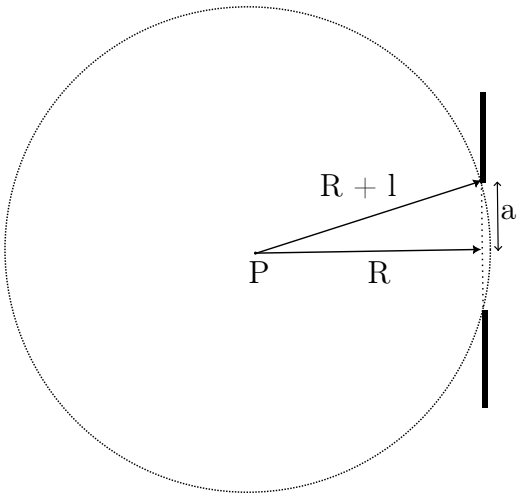

Figure 7.1: Schematic of an emitted wavefront from a point source P. A slit with an opening of $2a$ was placed in the wavefront.

To determine if a wavefront is sufficiently planar, we can derive an approximation [12]. Thus, considering the distance between the point source and the slit is R

$$(R+l)^2 = R^2 + a^2 \tag{7.1}$$

$$R^2 + 2Rl + l^2 = R^2 + a^2 \tag{7.2}$$

$$2Rl = a^2 - l^2 \tag{7.3}$$

$$R = \frac{a^2 - l^2}{2l} \tag{7.4}$$

Assuming that the waves at the slit are planar, $\lambda >> l$, thus $R, a >> l$,

$$R >> \frac{a^2}{2\lambda} \tag{7.5}$$

The above relationship between the distance between the point source and the slit R, the opening of the slit $2a$, and λ the wavelength of light is satisfied when the incident wavefront is approximately planar.

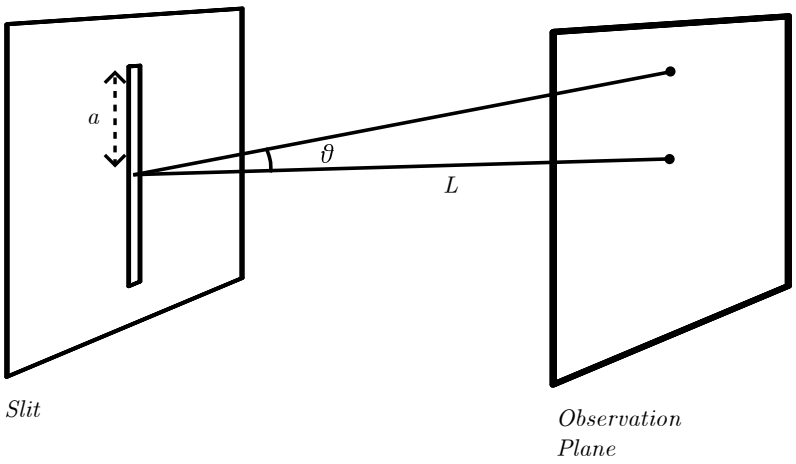

Figure 7.2: Schematic of a slit and observation plane for Fraunhofer Diffraction.

Thus, considering Fraunhofer Diffraction [12], the intensity distribution function through a slit is as follows,

$$I(\theta) = \frac{1}{2}\left(\frac{\epsilon_L 2a}{L}\right)^2 \left(\frac{\sin\beta}{\beta}\right)^2 \tag{7.6}$$

$$\beta \equiv 2a\pi \sin\theta \tag{7.7}$$

where, $I(\theta)$ is the intensity at the observation point, ϵ_L is the source strength per unit length, $2a$ is the opening of the slit, L is the distance between the slit and the observation point, and θ is the angular separation between the centre axis

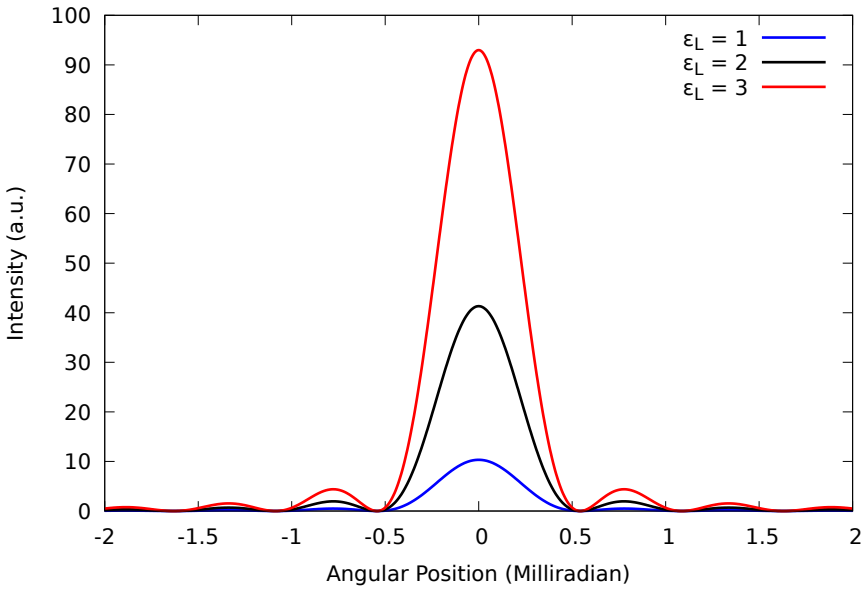

Figure 7.3: Numerically simulated the intensity distribution function after a slit. Distance between slit and observation point L: $2.2 \cdot 10^{-1}$ m, Wavelength λ: $5.435 \cdot 10^{-7}$ m, Opening of the slit $2a$: $1 \cdot 10^{-3}$ m

According to Fraunhofer diffraction (Equation 7.6), the only information about the point source P is captured in the ϵ_L. By increasing the source strength, the total intensity after the slit increased. But the overall shape remains the same.

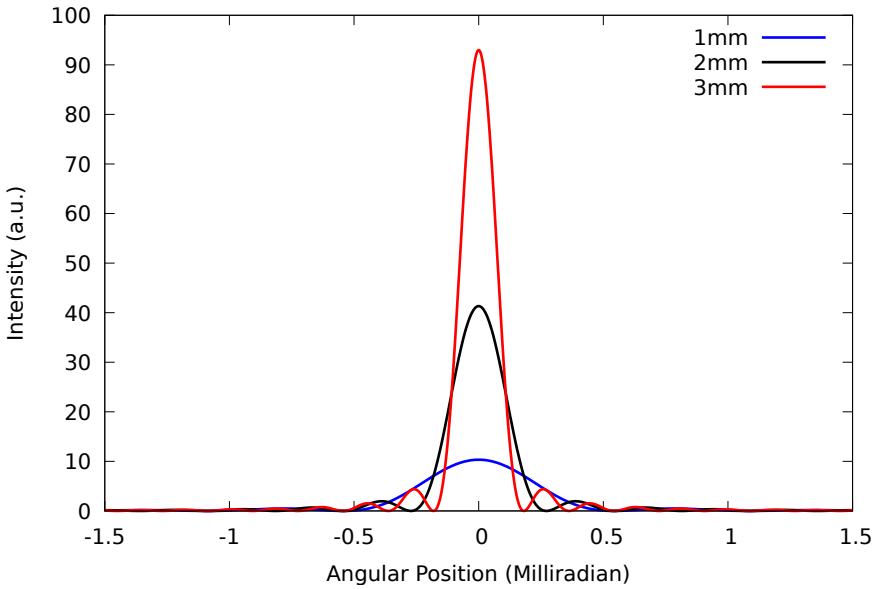

Figure 7.4: Numerically simulated intensity distribution function after a slit with various openings. Distance between slit and observation point L: $2.2 \cdot 10^{-1}$ m, Wavelength λ: $5.435 \cdot 10^{-7}$ m, Opening of the slit $2a$: $1 \cdot 10^{-3}$ m

7.2 Direct Measurement Methods

In this section, we consider direct measurement methods of a point light source and compare them against the Fraunhofer diffraction patterns in § 7.1. We investigated these methods in an attempt to gain more spatial information about a point light source instead of a single intensity measurement.

7.3 Imaging using camera

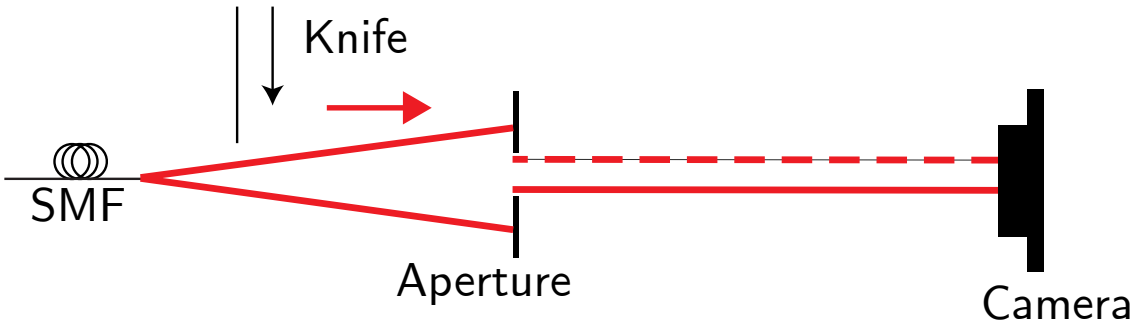

Figure 7.5: Light from a HeNe laser is coupled into a single-mode fiber. The output of a single-mode fiber is a spatially symmetrical diverging where a knife is used to generate radial asymmetries. A camera was placed after an iris to image the beam.

(a) No Knife (b) With Knife

Figure 7.6: Image taken after the aperture.

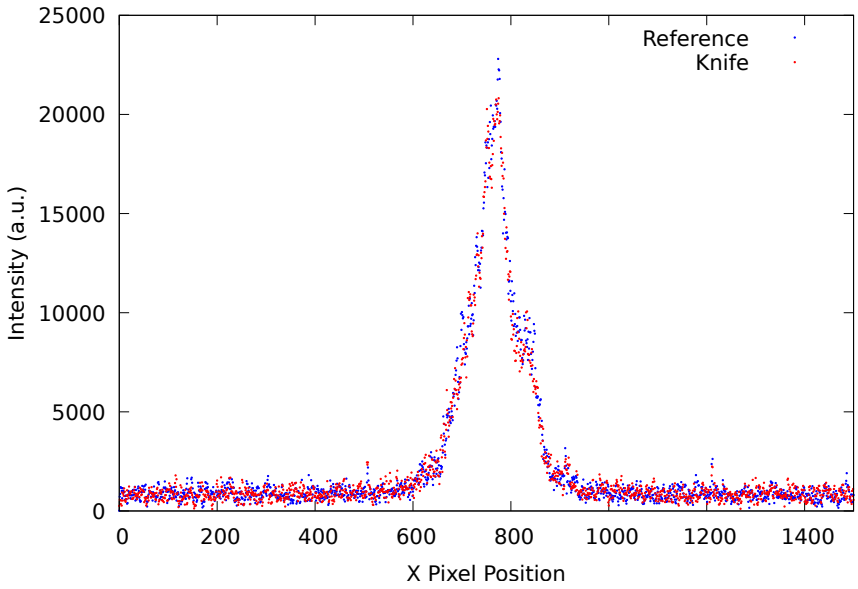

Figure 7.7: By taking the same row on both images and plotting the intensity. The intensity profiles look similar to Fraunhofer Diffraction, suggesting that the light source may be diffraction-limited. However, it may not show a significant difference where this is a knife obstructing the beam.

7.4 Imaging using slit translation

We investigated if there is any difference between a knife when it is near single-mode fiber (diffraction-limited) and a knife that is near the aperture (diameter about 1 mm). Using a slit to act as a filter such that the intensity of each position could be determined.

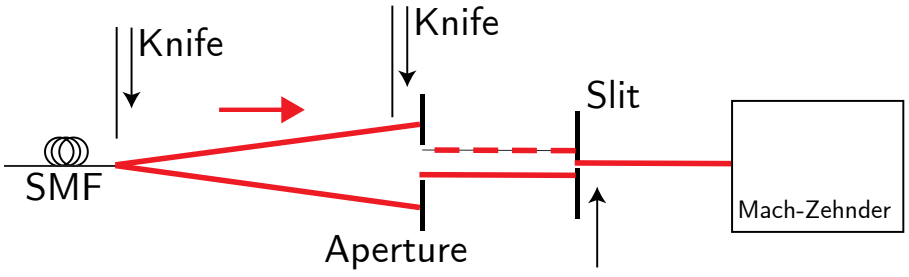

Figure 7.8: Schematic of experiment setup for slit translation. Light from a HeNe laser is focused into a single-mode fiber. After the diverging output of the interferometer, a knife partially obstructs part of the beam to generate radial asymmetry. Light after the slit was measured using APDs through the Mach-Zehnder interferometer with one of the paths blocked.

We characterise the knife obstruction at two positions to determine the position where this is a 10% percentage obstruction.

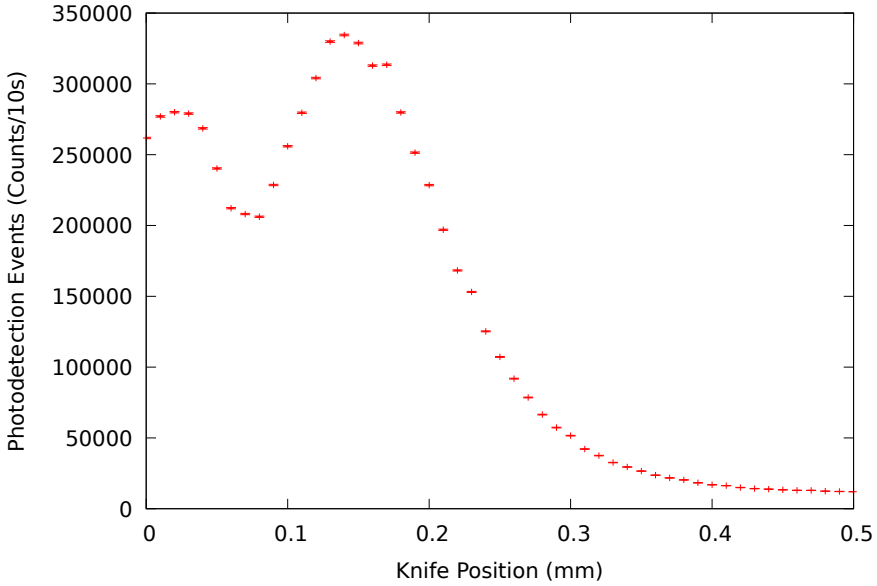

Figure 7.9: Characterisation of intensity against knife position to determine a position where both intensities decrease by 10% for comparison. Near single-mode-fiber

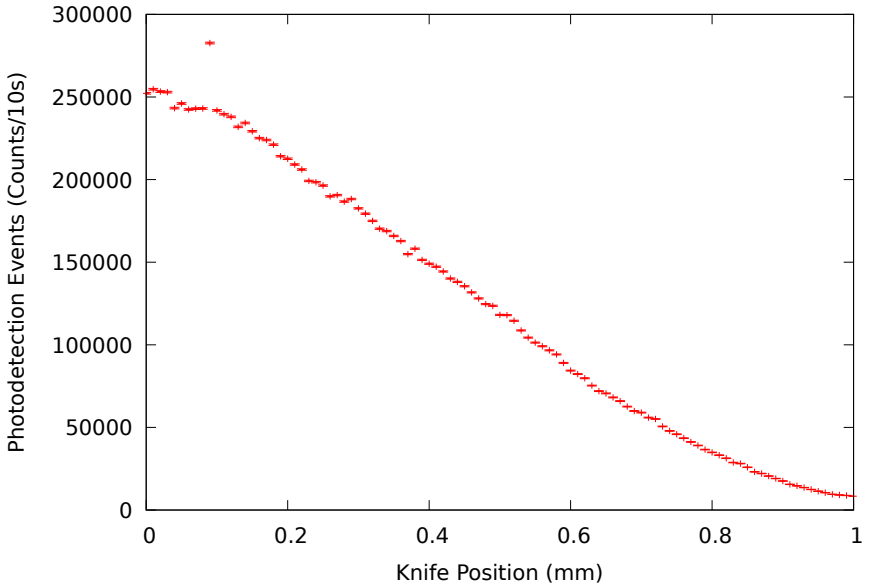

Figure 7.10: Characterisation of intensity against knife position to determine a position where both intensities decrease by 10% for comparison. Near aperture

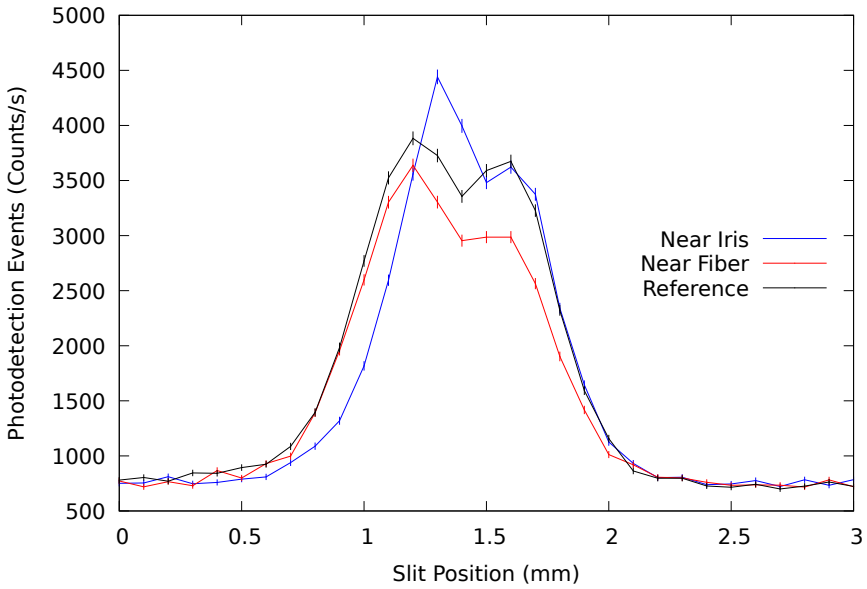

Figure 7.11: A slit with width of 0.004 in was translated across the beam after an aperture. The general shape of the intensity profiles does not follow Fraunhofer diffraction. A possibility is due to diffraction after the slit, which reduces coupling into the two APDs at the two outputs of the Mach-Zehnder interferometer.

7.5 Imaging using fiber translation

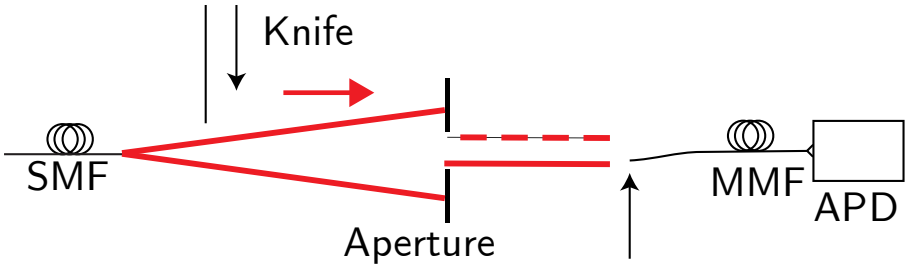

Figure 7.12: Schematic of experiment setup for fiber translation. Light from a HeNe laser is focused into a single-mode fiber. The diverging output of the single-mode fiber is partially obstructed by a knife to generate a radial asymmetric light source. After an aperture, a multi-mode fiber with a core diameter of 50 microns that is connected to an APD is translated across the beam.

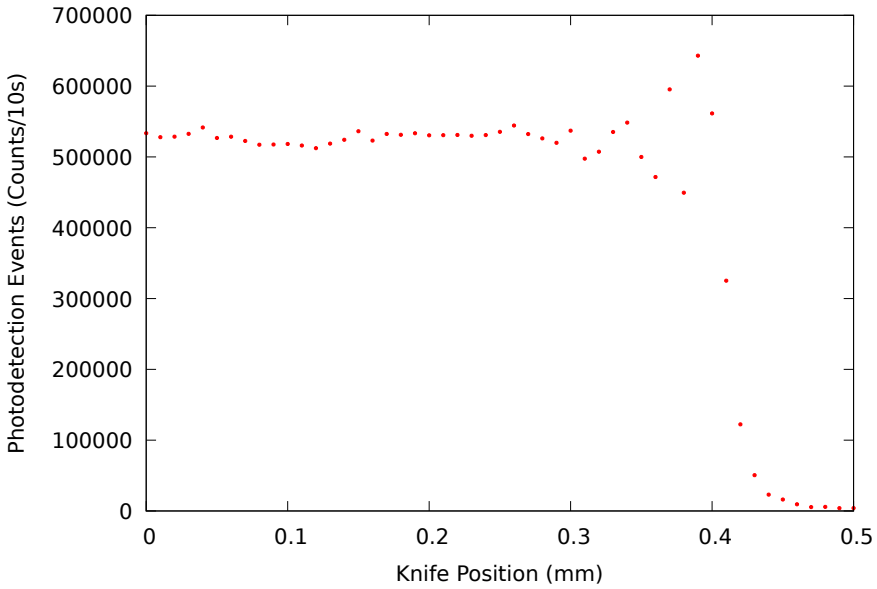

Figure 7.13: After translating the MMF and maximising photodetection events, we characterised intensity at each knife position

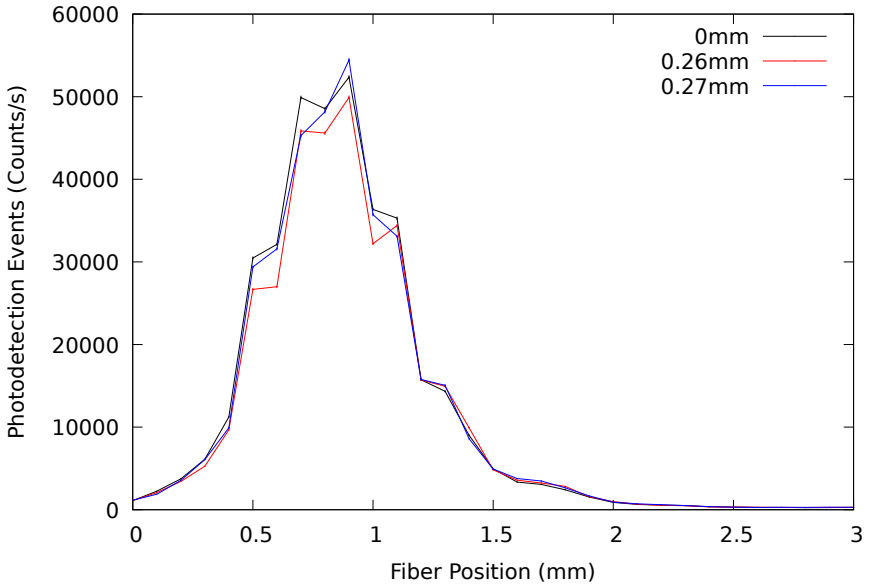

Figure 7.14: Imaging of asymmetric point light source using a multi-mode fiber that is linearly translated across the beam. The asymmetric point light source was generated using a partial knife obstruction.

7.6 Conclusion

A camera has pixel size on the order 3 microns. This provides a higher resolution compared to using a MMF with core diameter of 50 microns. However, a camera may not be able to capture the small change in power at the single photon level.

A potential solution to increase the resolution of the MMF and slit translation measurement is to translate them using smaller step sizes.

To effectively determine if these direct measurement methods are useful, they will need to be fitted to the Fraunhofer Diffraction function to determine if there are any changes between having a knife and a reference.

Chapter 8

Conclusion and Future Work

8.1 Conclusion

The project's goal is to extract spatial information, specifically radial asymmetric spatial information, from a diffraction-limited point light source using image inversion interferometry.

In Chapter 2, we discussed the reason for using a Mach-Zehnder interferometer. A Mach-Zehnder having two arms allows for one arm to act as a phase reference for the other such that the phase between the arms can be compared. In this case, an image inverter is inserted into one of the arms of the interferometer.

The image inverter is a pair of plano-convex lenses in a telescope configuration. Any incoming light is radially inverted along the optical axis. Hence, any radial asymmetrical properties between the two arms would not overlap at a beamsplitter and interfere. These radial asymmetrical properties are then separated into the two outputs of the interferometer and detected.

In Chapter 3, we investigate the properties of various light sources for interference. The HeNe laser has a noise of around $15\sqrt{N}$ compared to the $1.2\sqrt{N}$ of the Hg vapour lamp. In subsequent measurements, it is noted that the HeNe noise limited the smallest percentage obstruction resolvable in the measurements. As such, a replacement of HeNe is key for subsequent measurements.

While the Hg vapour lamp would be a good replacement, its 10^6 counts/s output may not be suitable for the measurement of radial asymmetric point light source at the object plane where there is a coupling loss of around 10^5.

As such, the detection of radial asymmetric point light sources would require a brighter light source, on the order of milliW similar to that of the HeNe laser, while

having a noise that is close to $\sqrt{N}$.

The coherence lengths of the light source used need to be longer than the optical path difference of the interferometer. Although the spectrum measurement for both HeNe and Hg vapour was spectrometer-limited, the linewidth for Hg was estimated to be about 10 cm based on Doppler broadening. Whereas, interference was seen with the HeNe laser, suggesting that the HeNe temporal coherence length is longer than the optical path difference.

In Chapter 4, we discussed on the generation of radially asymmetrical light source using a single mode fiber.

We choose to generate radial asymmetries through the use of an opaque obstruction. Thus, in an attempt to quantify the degree of asymmetry, we measured the change in power after the obstruction.

As such, the power and noise of the light source would limit the smallest measurable percentage obstruction.

However, using a change in power to quantify the degree of asymmetry assumes that the power distribution across the beam is uniform. Moreover, it may only work for obstructions that increase in obstruction area from the edge of the beam. This may not work for certain obstruction types, such as thin strips.

When the percentage obstruction of thin strips is at the maximum, the degree of asymmetry also depends on the position of the thin trip across the beam.

Hence, further analysis will be required to properly define the degree of asymmetry.

In Chapter 5, we investigate radial asymmetric light sources at the pupil plane. We numerically showed a regime in which image inversion's SNR is better than direct measurement.

However, to improve the statistics of our measurements, a stepper motor should have been used to translate the obstruction into the beam to better control the obstruction percentage. The step sizes of 0.0003125 /step allow for finer resolution than a standard micrometre screwgauge

In addition, measurements should also be taken against the obstruction position instead of in time to know the percentage obstruction at each position for repeatability.

Lastly, for all subsequent measurements, the visibility stability should have been quantified so that we can determine if the change in visibility is due to an obstruction or the visibility drifting, which affects the measurements' SNR.

In Chapter 6, we investigated radial asymmetrical point light sources at the object plane. While the goal was to investigate the spatial information of a diffraction-limited point source, mistakes were made in determining the aperture diameter. As such, the light source may not be diffraction-limited with respect to the aperture.

However, this wasn't a showstopper. One of the original intentions for diffraction-limited was spatial coherence, but since we are using single-mode fiber, the output is already spatially coherent.

In addition, there doesn't seem to be an increase in SNR for the direct measurement (total) case compared to the SNR (dark). This could be due to the stability of the HeNe laser again.

Switching the HeNe laser to Hg was not possible due to the 10^5 coupling losses between the single-mode fiber and after the iris.

The increasing oscillations present when a knife was translated into the beam may be the result of knife-edge diffraction. However, more investigation will be needed to quantify whether it is indeed knife-edge diffraction.

In the final Chapter 7, we investigated various forms of imaging methods of a diffraction-limited point source. A camera, a fiber, and a slit were used to image a diffraction-limited point source. Both the fibre and slit were translated to capture a 1-dimensional intensity distribution function.

While a camera with a pixel size of around 3 microns offers greater resolutions than the 50 microns MMF translated, a camera may not be able to capture small changes in power at the single photon level.

However, to effectively determine if direct measurement methods work, they should have been fitted to the Fraunhofer diffraction pattern to quantify the difference between situations when there is a knife and where there isn't

8.2 Future Research Directions

All in all, there are a few key issues that will need to be tackled for image inversion interferometry if the goal is to extract radial asymmetric spatial information from a

diffraction-limited point light source.

1. A light source that has output power on the order of milliW and has a noise of about $1\sqrt{N}$

2. Quantifying visibility stability such that it is similar to the duration of the measurement

3. Quantifying the degree of asymmetry such that there is a model to determine the expected outcome for each degree of asymmetry.

4. If asymmetric is generated using an obstruction, the smallest obstruction percentage is resolvable and other forms of obstruction to that may not have share edges.

Bibliography

1. Rayleigh, *The London, Edinburgh, and Dublin Philosophical Magazine and Journal of Science* **8**, 261–274, eprint: https://doi.org/10.1080/14786447908639684, (https://doi.org/10.1080/14786447908639684) (1879).
2. A. Schropp, R. Hoppe, J. Patommel, D. Samberg, F. Seiboth, S. Stephan, G. Wellenreuther, G. Falkenberg, C. G. Schroer, *Applied Physics Letters* **100**, ISSN: 0003-6951, (https://doi.org/10.1063/1.4729942) (2012).
3. A. Rosenauer, F. F. Krause, K. Müller, M. Schowalter, T. Mehrtens, *Physical review letters* **113**, 096101 (2014).
4. "The European Extremely Large Telescope Construction Proposal", Report (European Southern Observatory), (https://www.eso.org/sci/facilities/eelt/docs/e-elt_constrproposal.pdf).
5. S. W. Hell, J. Wichmann, *Optics Letters* **19**, 780–782, (https://opg.optica.org/ol/abstract.cfm?URI=ol-19-11-780) (1994).
6. E. Betzig, G. H. Patterson, R. Sougrat, O. W. Lindwasser, S. Olenych, J. S. Bonifacino, M. W. Davidson, J. Lippincott-Schwartz, H. F. Hess, *Science* **313**, 1642–1645, (https://www.science.org/doi/abs/10.1126/science.1127344) (2006).
7. M. Tsang, R. Nair, X.-M. Lu, *Phys. Rev. X* **6**, 031033, (https://link.aps.org/doi/10.1103/PhysRevX.6.031033) (3 Aug. 2016).
8. R. Nair, M. Tsang, *Optics Express* **24**, 3684–3701, (https://opg.optica.org/oe/abstract.cfm?URI=oe-24-4-3684) (2016).
9. Z. S. Tang, K. Durak, A. Ling, *Opt. Express* **24**, 22004–22012, (https://opg.optica.org/oe/abstract.cfm?URI=oe-24-19-22004) (Sept. 2016).
10. A. A. Michelson, *American Journal of Science* **s3-34**, 333–345, ISSN: 0002-9599 (1887).

11. L. Mach, *Zeitschrift für Instrumentenkunde* **12**, 89 (1892).

12. E. Hecht, "Optics", (Pearson, 2014), ISBN: 9781292021577, (https://books.google.com.sg/books?id=ZakzngEACAAJ).

13. K. Wicker, R. Heintzmann, *Optics Express* **15**, 12206–12216, (https://opg.optica.org/oe/abstract.cfm?URI=oe-15-19-12206) (2007).

14. M. Fox, "Quantum Optics: An Introduction", (OUP Oxford, 2006), ISBN: 9780198566731, (https://books.google.com.sg/books?id=2_ZP-LDF9jkC).

15. "Cylindrical Helium Neon Laser Systems", Report (Melles Griot), (https://physlab.org/wp-content/uploads/2016/03/Laser_hene_melles_griot_specs.pdf).

16. N. Ortiz, "OceanOptics Wavelength Calibration Data Sheet", Report, (https://qoptics.quantumlah.org/wiki/images/5/50/Oceanopticscalib.pdf).

17. "Optical Interference Filters", Catalog, 2012, (https://www.spotimaging.com/downloads/public/pdf/omega_optical_filters.pdf).

18. W. D. B. Hermann Haken Hans Christoph Wolf, "The Physics of Atoms and Quanta", (Springer Berlin, Heidelberg, ed. 7, 2005), p. 520, ISBN: 978-3-540-20807-5.

19. J. D. Pickering, "Knife Edge Scanning for Beam Profiling", Report, (https://jamesdpickering.com/pdfs/knife_edge_profiler.pdf).

20. (https://www.thorlabs.com/newgrouppage9.cfm?objectgroup_id=944&pn=F220FC-A).

21. S. Y. Foo, Final Year Project Thesis, 2022.

22. S. Y. Foo, M. Z. Koh, X. J. Yeo, J. S. Hwang, C. Kurtsiefer, P. K. Tan, "Dark-field separation of optical modes in a thermal point source", (SPIE, 2023), vol. 12740, (https://doi.org/10.1117/12.2675829).

23. (https://www.flir.com/globalassets/imported-assets/document/datasheet_cm3_u3_31s4.pdf).